iScience

CellPress
OPEN ACCESS

Article

Adipocyte hypertrophy associates with *in vivo* postprandial fatty acid metabolism and adipose single-cell transcriptional dynamics

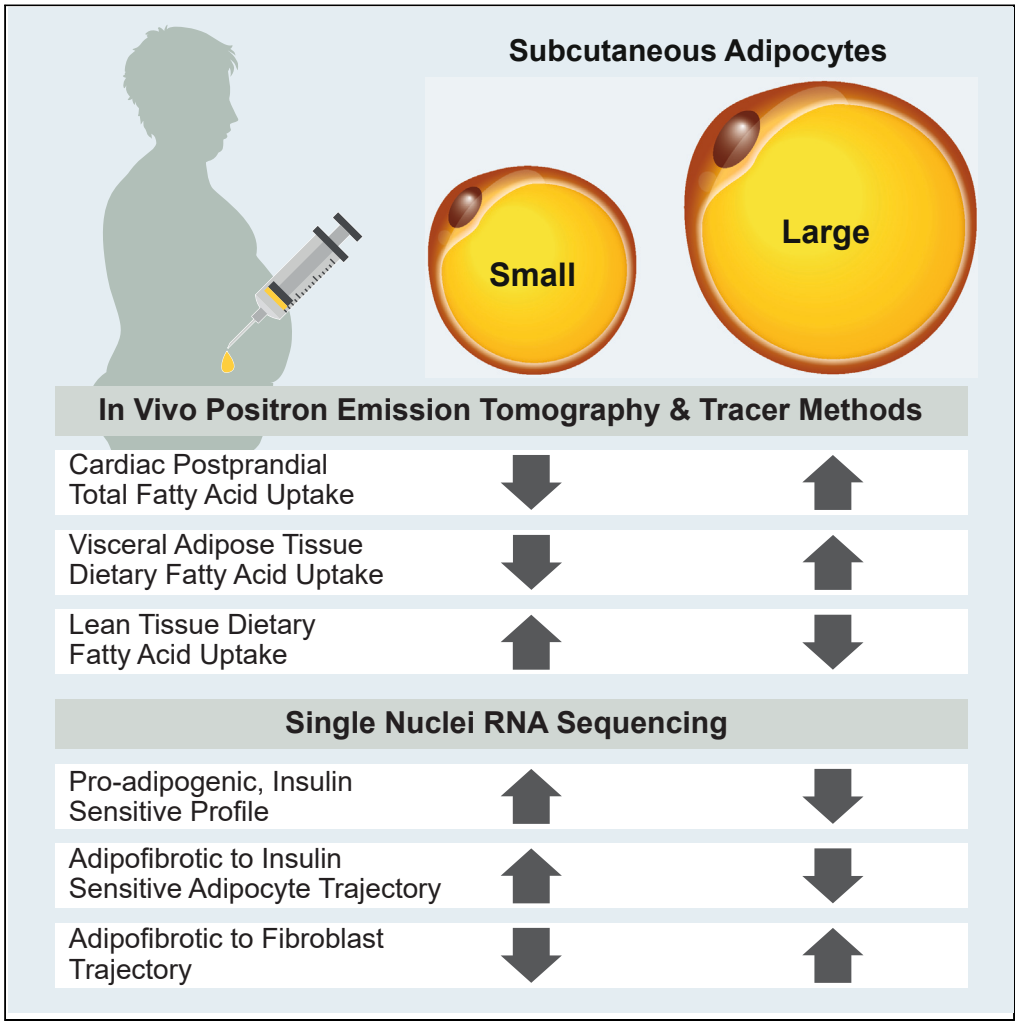

Run Zhou Ye, Emilie Montastier, Frédérique Frisch, ..., Nicolas Gévry, André Tchernof, André C. Carpentier

andre.carpentier@usherbrooke.ca

Highlights

Adipocyte hypertrophy associates independently of obesity with:
Higher total postprandial fatty acid flux to the heart

Higher dietary fatty acid uptake in visceral fat, but lower uptake in lean tissues

Reduced adipogenic and insulin sensitivity transcriptomic profile

Change in differentiation trajectories of adipocytes and fibroadipogenic cells

Ye et al., iScience *27*, 108692
January 19, 2024
https://doi.org/10.1016/j.isci.2023.108692

iScience

CellPress
OPEN ACCESS

Article

Adipocyte hypertrophy associates with *in vivo* postprandial fatty acid metabolism and adipose single-cell transcriptional dynamics

Run Zhou Ye,[1] Emilie Montastier,[1] Frédérique Frisch,[1] Christophe Noll,[1] Hugues Allard-Chamard,[1] Nicolas Gévry,[2] André Tchernof,[3] and André C. Carpentier[1,4,5,*]

SUMMARY

Adipocyte hypertrophy is associated with metabolic complications independent of obesity. We aimed to determine: 1) the association between adipocyte size and postprandial fatty acid metabolism; 2) the potential mechanisms driving the obesity-independent, hypertrophy-associated dysmetabolism *in vivo* and at a single-cell resolution. Tracers with positron emission tomography were used to measure fatty acid metabolism in 40 men and women with normal or impaired glucose tolerance (NCT02808182), and single nuclei RNA-sequencing (snRNA-seq) to determine transcriptional dynamics of subcutaneous adipose tissue (AT) between individuals with AT hypertrophy vs. hyperplasia matched for sex, ethnicity, glucose-tolerance status, BMI, total and percent body fat, and waist circumference. Adipocyte size was associated with high postprandial total cardiac fatty acid uptake and higher visceral AT dietary fatty acid uptake, but lower lean tissue dietary fatty acid uptake. We found major shifts in cell transcriptomal dynamics with AT hypertrophy that were consistent with *in vivo* metabolic changes.

INTRODUCTION

Adipose tissue (AT) hypertrophy can be viewed as the result of a positive energy imbalance coupled with inefficient expansion via hyperplasia.[1] Therefore, in response to chronic nutritional excess, AT with low potential for adipogenesis may expand through hypertrophy, that is the enlargement of the fat cell lipid droplet. AT in the subcutaneous region appears to be the first tissue to expand in response to energy excess.[2,3] As subcutaneous AT reaches its limit for expansion, excess lipid may still continue to accumulate in visceral AT, liver, skeletal muscles and the heart. This subcutaneous AT expandability may vary between individuals, leading to varied ectopic fat accumulation and metabolic endpoints despite similar total body fat. We have recently shown that postprandial fatty acid efflux from AT was offset by increased trapping of dietary fat by AT during overfeeding in healthy individuals.[4] However, this increased dietary fatty acid (DFA) trapping insufficiently curbs increased postprandial uptake of fatty acids by lean tissues in individuals with prediabetes.[5] No data exist regarding the relationships between adipocyte hypertrophy and *in vivo* measurements of whole-body metabolism of both nonesterified fatty acid (NEFA) and chylomicron-derived dietary fatty acid. Furthermore, mechanisms of AT hypertrophy-associated dysmetabolism that are independent of the level of obesity need to be better defined at a cellular level. Yet, most single-cell RNA-sequencing (scRNA-seq) studies on white AT did not investigate mature adipocytes,[6–10] because their greater lipid content and fragility preclude microfluidic single-cell capture. An emerging method for including mature adipocytes consists of extracting cell nuclei from whole AT samples and perform snRNA-seq.[11–13] snRNA-seq is highly correlated with classic scRNA-seq.[14] Furthermore, the use of flash-frozen human AT for snRNA-seq is promising, because such method would enable temporal dissociation between biopsy collection and single-nuclei capture, as well as the use of existing large AT biobanks for subsequent single-nuclei analysis.

In the present study, we assessed the associations between subcutaneous adipocyte size and systemic and organ-specific fatty acid metabolism in 40 men and women with normal or impaired glucose tolerance (IGT) measured using a combination of oral and i.v. tracers with positron emission tomography. In addition, we have performed snRNA-seq using flash-frozen human AT. To determine changes in single-cell transcriptome associated with AT hypertrophy, but independent of the level of obesity, we selected participants that differed significantly in fat cell size but with the same total and percent fat mass, BMI, waist circumference, sex, ethnicity, and glucose tolerance status. Differences in transcriptional dynamics and developmental trajectory detected *ex vivo* were also compared with changes in AT distribution, *in vivo* metabolic endpoints and AT lipid metabolism measured by whole-body PET/CT imaging.

[1]Division of Endocrinology, Department of Medicine, Centre de recherche du CHUS, Université de Sherbrooke, Sherbrooke, QC J1H 5N4, Canada
[2]Department of Biology, Université de Sherbrooke, Sherbrooke, QC J1K 2R1, Canada
[3]Québec Heart and Lung Research Institute, Laval University, Québec, QC G1V 4G5, Canada
[4]Department of Nuclear Medicine and Radiobiology, Centre de Recherche du CHUS, Université de Sherbrooke, Sherbrooke, QC J1H 5N4, Canada
[5]Lead contact
*Correspondence: andre.carpentier@usherbrooke.ca
https://doi.org/10.1016/j.isci.2023.108692

Table 1. Predictors of adipose tissue insulin resistance, rates of hepatic and cardiac NEFA metabolism, adipose and lean tissue DFA partitioning in multivariate analysis

	β-coefficient	*t*-value	p-value	R^2	*Sig.*
Adipose tissue insulin resistance					
Rank ATIRI					
Predictors:				0.18	0.01
(Constant)		−3.249	0.003		
Adipocyte diameter	0.419	2.612	0.014		
Log Fasting ADIPO-IR					
Predictors:				0.40	0.0003
(Constant)		5.406	0.000		
1/BMI	−0.580	−4.250	0.000		
Sex (F = 1/M = 0)	0.275	2.016	0.052		
Log Postprandial ADIPO-IR					
Predictors:				0.68	4×10^{-7}
(Constant)		1.361	0.184		
1/BMI	−0.424	−3.422	0.002		
Adipocyte diameter	0.297	2.536	0.017		
Glucose tolerance (NGT = 0/IGT = 1)	0.319	2.795	0.009		
Age	−0.205	−1.908	0.066		
Adipose and lean tissue DFA partitioning					
SCAT DFA partitioning					
Predictors:				0.20	0.006
(Constant)		5.046	0.00002		
1/BMI	−0.452	−2.909	0.006		
VAT DFA partitioning					
Predictors:				0.11	0.04
(Constant)		−0.408	0.686		
Adipocyte diameter	0.342	2.094	0.044		
Lean tissue DFA partitioning					
Predictors:				0.49	0.00002
(Constant)		7.753	8×10^{-9}		
1/BMI	0.511	3.562	0.001		
Adipocyte diameter	−0.293	−2.046	0.049		
Rates of hepatic and cardiac NEFA metabolism					
Log Cardiac NEFA uptake					
Predictors:				0.21	0.006
(Constant)		−7.224	0.000		
Adipocyte diameter	0.458	2.959	0.006		
Log Cardiac NEFA oxidation					
Predictors:				0.23	0.004
(Constant)		−7.282	0.000		
Adipocyte diameter	0.476	3.110	0.004		
Log Hepatic NEFA uptake					
Predictors:				0.15	0.02

(*Continued on next page*)

Table 1. *Continued*

	β-coefficient	*t*-value	p-value	R^2	*Sig.*
(Constant)		−6.488	0.000		
Adipocyte diameter	0.380	2.362	0.024		
Log Hepatic NEFA oxidation					
Predictors:				0.14	0.02
(Constant)		−5.799	0.000		
Adipocyte diameter	0.380	2.357	0.024		
Total postprandial NEFA and DFA uptake					
Log cardiac U_{NEFA}					
Predictors:				0.15	0.02
(Constant)		−0.525	0.603		
Adipocyte diameter	0.382	2.371	0.024		
Log cardiac U_{TFA}					
Predictors:				0.13	0.03
(Constant)		−0.140	0.890		
Adipocyte diameter	0.363	2.305	0.027		

Potential predictors tested for multivariate regression: 1/BMI, adipocyte diameter, age, sex, and glucose tolerance. ATIRI, adipose tissue insulin-resistance index; ADIPO-IR, adipose tissue insulin-resistance; BMI, body mass index; DFA, dietary fatty acid; F, female; M, male; NEFA, non-esterified fatty acid; NGT, normal glucose tolerance; IGT, impaired glucose-tolerance; TG, triglyceride; SCAT, subcutaneous adipose tissue; VAT, visceral adipose tissue; U_{NEFA}, total uptake of circulating non-esterified fatty acids; U_{TFA}, uptake of all fatty acids.

RESULTS

Participant characteristics

This article reports a pre-specified secondary outcome measurement (abdominal SCAT adipocyte volume) and exploratory analyses of the relationship of this measurement with postprandial fatty acid metabolic outcomes of NCT02808182. Data from this study have partly been reported previously.[4,5] A cohort of 40 individuals who underwent SCAT biopsy and extensive metabolic testing was used to select two matched participants. Twenty of these subjects had normal glucose tolerance, while 19 had IGT.[5] One additional subject had type 2 diabetes based on fasting glucose over 6.9 mmol/L on at least two occasions after screening and was included in the analyses. The characteristics of the 40 participants are detailed in Table S1.

Relationships between adipocyte size and variations in whole-body adipose tissue distribution, *in vivo* metabolic endpoints, and changes in *in vivo* adipose tissue lipid metabolism measured by whole-body PET/CT imaging

Table S2 shows the univariate associations between abdominal SCAT mean adipocyte volume and demographic, anthropometric and postprandial fatty acid metabolic parameters. Adipocyte diameter was significantly associated with decreased Matsuda index, fasting leptin, fasting TG, and postprandial NEFA $_{90\text{-}120\ min}$. As shown in Table 1, the Adipose Tissue Insulin Resistance Index (ATIRI)[15] was correlated only with adipocyte diameter. Fasting ADIPO-IR[16] was independently predicted by BMI and female sex, whereas postprandial ADIPO-IR[17] was independently associated with BMI, adipocyte diameter, IGT, and younger age.

To measure *in vivo* postprandial partitioning of DFA in the liver, heart, muscles, and subcutaneous and visceral AT, we performed whole-body PET/CT with the oral administration of [^{18}F]-FTHA, as previously described.[4,5,18] DFA uptake in AT was measured based on the CT segmentation maps generated using deep learning as described in.[19] Subcutaneous AT DFA partitioning was marginally associated with adipocyte diameter (Figure 1A). This positive correlation was possibly the result of increased BMI and subcutaneous AT volume with adipocyte hypertrophy, because BMI was the only independent predictor of subcutaneous AT DFA partitioning (Table 1) and subcutaneous AT DFA partitioning was not associated with adipocyte size once adjusted for BMI ($r = 0.14$, $p = 0.4$). Adipocyte size was associated with visceral AT DFA partitioning (Figure 1B) and with reduced lean tissue DFA partitioning (Figure 1C), independently of BMI (Table 1).

To measure rates of *in vivo* hepatic and cardiac uptake and metabolism of circulating NEFA (in μmol/ml/min), we performed thoracic dynamic PET/CT imaging with the IV administration of [^{11}C]-palmitate 90 min after a standard mixed meal.[5] Analyses in our entire cohort of 40 subjects showed that adipocyte diameter was the only predictor of the rates of cardiac and hepatic NEFA uptake and oxidation 90 to 120 min after the meal (Table 1). In addition, fat cell size was also correlated with increased liver fat content assessed by hepatic CT radio-density ($r = -0.35$, $p = 0.03$).

The rates of hepatic and cardiac NEFA uptake were integrated over 6 h postprandially (in mmol/organ/6h). Total NEFA uptake values were combined with total postprandial hepatic and cardiac DFA uptake after excluding the intestinal retention of DFA to compute total

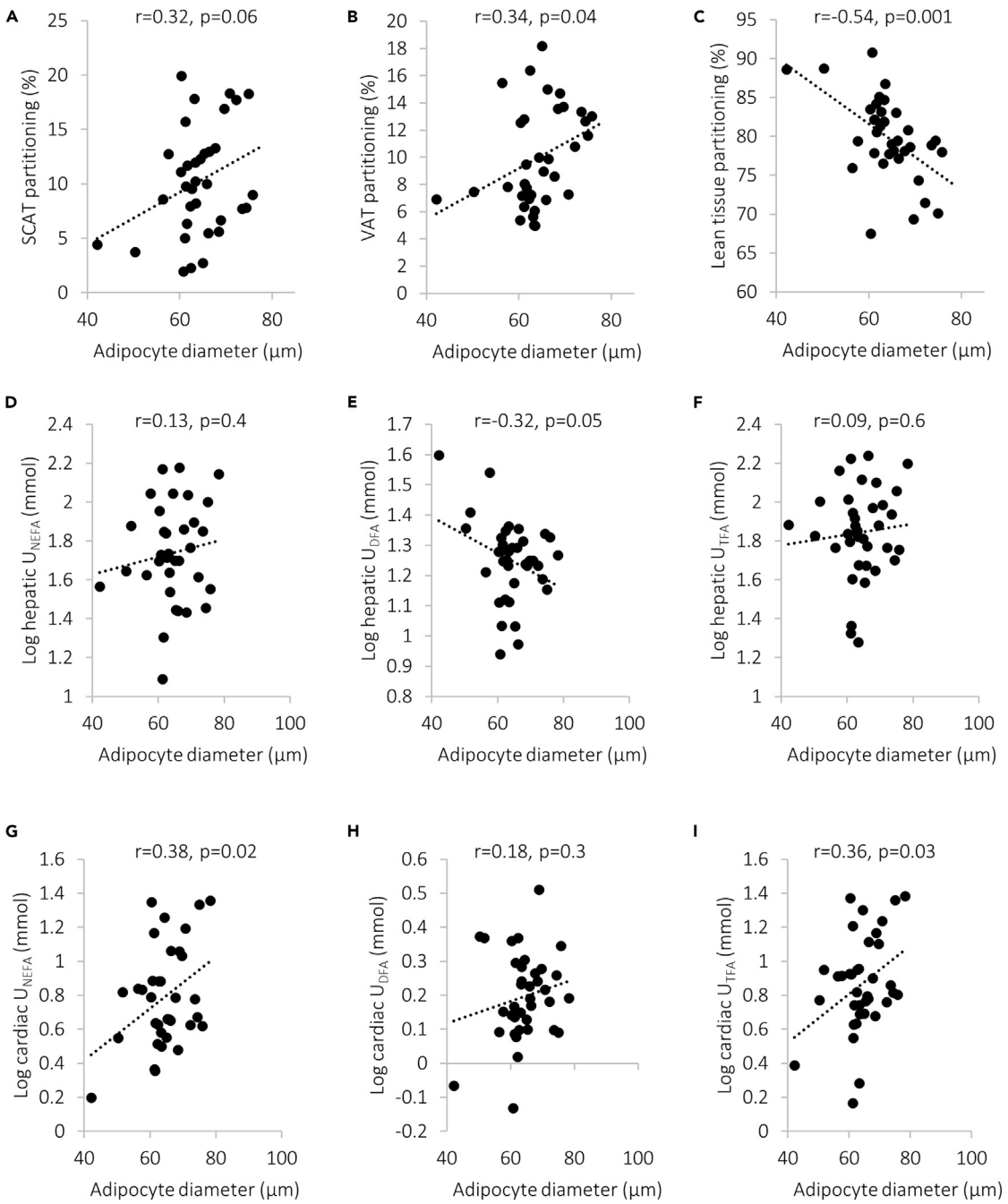

Figure 1. Association of adipocyte diameter with organ-specific fatty acid metabolism

(A) Association with dietary fatty acid partitioning in subcutaneous adipose tissue.

(B) Association with dietary fatty acid partitioning in visceral adipose tissue.

(C) Association with dietary fatty acid partitioning in lean tissues.

(D) Association with 6-h postprandial uptake of nonesterified fatty acid in the liver.

(E) Association with 6-h postprandial uptake of dietary fatty acids in the liver.

(F) Association with 6-h total fatty acid uptake in the liver.

(G) Association with 6-h postprandial uptake of nonesterified fatty acid in the heart.

(H) Association with 6-h postprandial uptake of dietary fatty acids in the heart.

(I) Association with 6-h total fatty acid uptake in the heart. SCAT, subcutaneous adipose tissue; U_{DFA}, total uptake of dietary fatty acids; U_{NEFA}, total uptake of circulating non-esterified fatty acids; U_{TFA}, uptake of all fatty acids; VAT, visceral adipose tissue; Pearson's r for variables with normalized distribution.

postprandial uptake of all sources of fatty acids by the heart and liver, as we recently described.[5] As shown in Figure 1 and Table 1, adipocyte diameter was positively correlated with total postprandial uptake of NEFA (Figure 1G) and all sources of fatty acids (Figure 1I) by the heart and tended to be associated with reduced total postprandial uptake of DFA by the liver (Figure 1E). Forcing glucose tolerance status in the regression model did not change the association between adipocyte size and lean tissue fatty acid uptake and metabolism (Table S3).

Single nuclei RNA-sequencing of matched participants

For snRNA-seq, we used SCAT biopsy samples from the two matched participants for BMI, waist circumference and total fat mass, but with different abdominal subcutaneous fat cell size (FCS) (see STAR methods, Figures S1 and S2). After fluorescence-activated cell sorting (FACS) purification, we recovered 37 000 nuclei from a 240 mg and 33 000 nuclei from a 100 mg frozen biopsy sample from the participant with adipocyte hypertrophy (high FCS, 76 μm) and hyperplasia (low FCS, 60 μm), respectively. Approximately 10 000 and 9 000 nuclei were loaded for single-nuclei capture for the hypertrophic and hyperplasic AT, respectively. After quality control by removing empty droplets, doublets, low-quality nuclei and genes with low expression (see STAR methods), filtered nuclei from the two biopsies were combined for variable feature extraction, dimension reduction, UMAP mapping,[20] and clustering (Figure 2A).

Whole-body at distribution, *in vivo* metabolic endpoints, and *in vivo* at lipid metabolism of matched participants

Compared to the individual with AT hyperplasia (Table S4), the matched participant with AT hypertrophy displayed insulin resistance (*i.e.*, lower Matsuda index, 3.88 vs. 8.19; higher HOMA-IR, 4.99 vs. 1.37), AT insulin resistance (*i.e.*, higher fasting[16] [43.5 vs. 17.0] and postprandial ADIPO-IR[17] [42.4 vs. 9.3]; higher ATIRI[15] [0.77 vs. −3.09]), higher fasting plasma insulin (134.6 vs. 52.7 pmol/L), leptin (8.2 vs. 2.4 ng/mL), TG (1.5 vs. 0.70 mmol/L) and NEFA $_{90\text{-}120}$ min (0.20 vs. 0.04 mmol/L), and lower plasma adiponectin level (7520 ng/mL vs. 9734 ng/mL).

As shown in Figures 2F and 2G although our two matched participants both had similar total AT volume (22.5 L [hypertrophy] vs. 21.3 L [hyperplasia]), subcutaneous AT volume was lower (16.8 L vs. 19.1 L) whereas visceral AT volume was higher (5.7 L vs. 2.3 L) in the individual with subcutaneous AT hypertrophy compared to the participant with subcutaneous AT hyperplasia. This difference reflects enhanced visceral AT expansion possibly due to a less expanded hypertrophic subcutaneous AT. Compared to the participant with subcutaneous AT hyperplasia, the matched individual with AT hypertrophy displayed lower subcutaneous AT DFA partitioning (9.0% vs. 11.1%) but higher DFA partitioning in the visceral AT (13.0% vs. 5.4%) (Figures 2H and 2I).

Compared to the participant with subcutaneous AT hyperplasia (Table S4), the individual with AT hypertrophy showed higher rates of cardiac NEFA uptake (0.043 vs. 0.007 μmol/L/min), oxidation (0.021 vs. 0.007 μmol/L/min), and esterification (0.021 vs. 0.0006 μmol/L/min), and of hepatic NEFA uptake (0.087 vs. 0.017 μmol/L/min), oxidation (0.035 vs. 0.005 μmol/L/min), esterification (0.053 vs. 0.012 μmol/L/min), and TG release (0.002 vs. 0.0009 μmol/L/min). Accordingly, Figures 2J and 2K illustrate cumulated cardiac and hepatic ^{11}C-palmitate activity over 30 min following tracer injection and show that the participant with AT hypertrophy had higher tracer activity in the heart and liver.

Single nuclei RNA-sequencing revealed major cell types in hypertrophic and hyperplasic subcutaneous adipose tissue

Five major cell types were identified: clusters 1, 2, 3, 4, and 5 were annotated as adipocytes, endothelial cells, fibroadipogenic cells (FAC), immune cells, and pericytes, respectively (Figure 2B). As expected, adipocytes expressed significantly higher levels of adipokines (*LEP* and *ADIPOQ*) and enzymes implicated in lipid metabolism (e.g., *PNPLA2*, *LIPE*, and *FASN*) compared to other cell types (Figure 2C), while FACs were characterized by the expression of collagen (e.g., *COL6A3* and *COL1A1*) and fibroblast-specific genes (*DCN* and *PDGFRA*).[21] Endothelial cells were characterized by endothelial cell-marker genes (e.g., *ESAM*,[22] *FLT1*,[23] *VWF*,[24] and *EGFL7*[25]) and pericytes by the expression of contractile proteins (e.g., *MYO1B* and *ACTA2*) and *RGS5*, a pericyte-specific gene.[26] Finally, immune cells demonstrated high expression of immune cell markers (e.g., *TLR4*, *CD37*, *CD68*, *CD163*, *FCGR2B*, *CSF1R*, and *PTPRC*). Furthermore, Figure 2C also shows that the measured expression levels of marker genes were constant across both biopsy samples, suggesting that our method generates consistent results between replicates.

Adipocyte hypertrophy/hyperplasia is associated with variation in cell distribution across different cell types

The UMAP projections on Figure 2D shows that hypertrophied AT is infiltrated by a greater number of immune cells compared to the hyperplasic adipose tissue. Figure 2D also illustrates that fat cell hypertrophy is associated with adipocytes that are transcriptionally distinct from those found in hyperplasic AT. Because the total number of profiled nuclei varied across samples, the fraction of each cell type was computed (Figure 2E), showing that the fraction of immune cells is almost doubled (1.9 times) in the hypertrophied AT.

Adipose tissue hypertrophy/hyperplasia is associated with shifts in transcriptionally distinct adipocyte subpopulations

Adipocytes were separated from other cell types and clustered, resulting in three subpopulations of fat cells with distinct transcriptional programs (Figure 3A). As shown in Figure 3B, insulin-resistant adipocytes (IRA) expressed higher mRNA levels of enzymes implicated in lipid metabolism (e.g., *LPL*, *CD36*, *LIPE*, *FASN*, and *DGAT*) as well as factors associated with reduced adipogenesis, enhanced inflammation, and insulin resistance (e.g., *FABP4*,[27–29] *CD36*,[30,31] and *ANGPTL2*[32–34]). In contrast, insulin-sensitive adipocytes (ISA) were characterized by higher expression of genes involved in insulin sensitivity (*PPARG*,[35,36] *IRS1*,[37–40] and *IGFBP5*[41–43]), adipogenesis (*PPARG* and *CEBPB*[44]), and beta-oxidation (*ACSL1*). The third subpopulation of adipocytes was differentiated by the expression of transcriptional factors, ribosomal

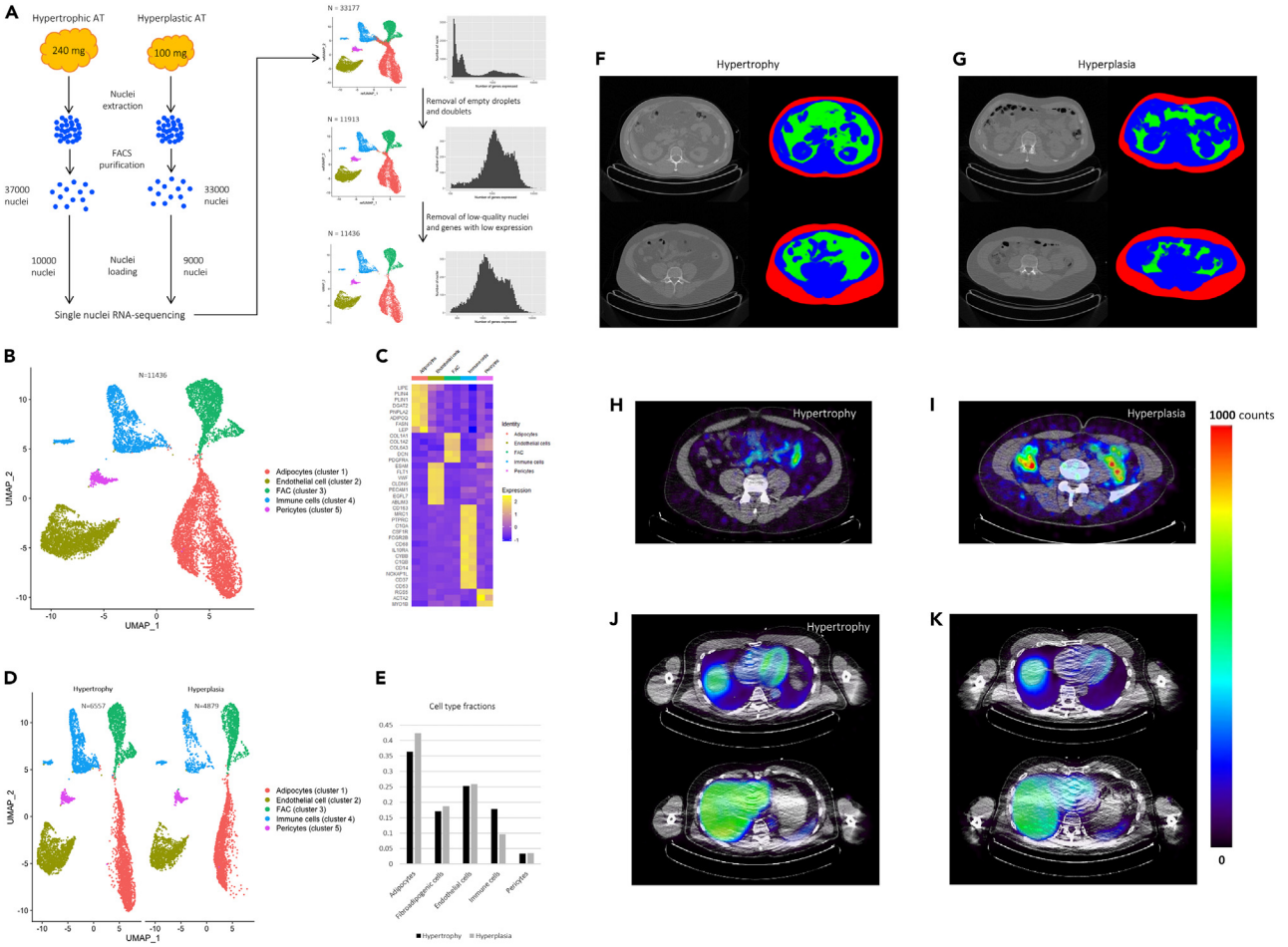

Figure 2. Comparision of adipose tissue single nuclei RNA sequencing characteristics, visceral adipose tissue, and fatty acid metabolism of matched subjects with hypertrophic *vs* hyperplasic adipocytes

(A) Overview of single nuclei experimental procedure and data quality control pipeline.

(B) UMAP projection of adipose tissue nuclei showing the major AT cell types.

(C) Level of expression of cell type maker genes in nuclei of the two biopsies (left square: hypertrophic biopsy, right square: hyperplasic biopsy).

(D) Comparison of UMAP projections between the hypertrophic and hyperplasic adipose tissues.

(E) Differences in cell type fractions between the hypertrophic and hyperplasic adipose tissues.

(F and G) Transverse computed tomography images and segmentation maps generated by deep convolutional neural network, showing different quantities of visceral adipose tissue (in green) and subcutaneous adipose tissue (in red) between the participants with subcutaneous adipose tissue hypertrophy (F) vs. hyperplasia (G).

(H and I) Abdominal transverse computed tomography images overlayed with [^{18}F]-fluorothiaheptadecanoic acid positron emission tomography images showing dietary fatty acid distribution in the participant with subcutaneous adipose tissue hypertrophy (H) and in the participant with subcutaneous adipose tissue hyperplasia (I).

(J and K) Thoracic transverse computed tomography images overlayed with cumulative [^{11}C]-palmitate activity measured by dynamic thoracic positron emission tomography over 5 to 30 min following tracer injection in the participant with subcutaneous adipose tissue hypertrophy with (J) and in the participant with subcutaneous adipose tissue hyperplasia (K). FAC, fibroadipogenic cells.

proteins, and genes involved in adipogenesis (*ZNF638*,[45,46] *FGFR1*,[47,48] *LRP1*,[49] *ACSS2*,[50] and *GSK3B*[51,52]) as well as insulin sensitivity (*INSR*[53,54] and *LRP5*[55]) and was, therefore, annotated as transcriptionally active developing adipocytes (TADA).

Differences in adipocyte subpopulations and transcriptional profiles between hypertrophy and hyperplasia are highlighted in Figure 3C, which illustrates a dramatic shift from a dominance of IRA in hypertrophied AT to a preponderance of ISA with AT hyperplasia. Figure 3D shows that IRA constitute 80% of all adipocytes in hypertrophied AT but are nearly absent in AT hyperplasia, while the reverse is true for the ISA subpopulation. Furthermore, compared to hypertrophied AT, the sample with AT hyperplasia contains a higher fraction of TADA. The higher concentration of TADA in hyperplasic vs. hypertrophied AT is even more noticeable when the number of adipocytes is expressed *per* volume of AT (Figure 3E).

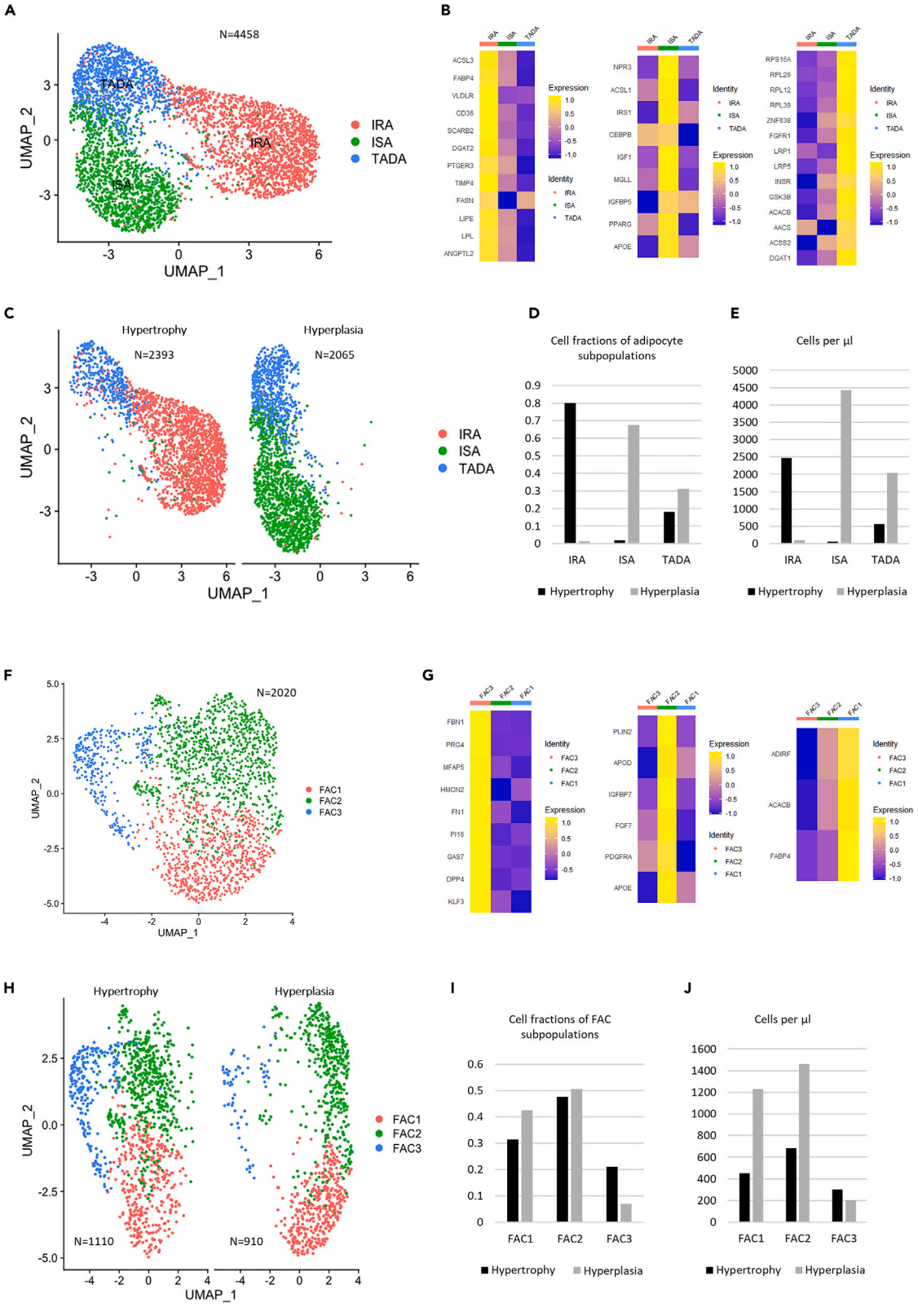
A
N=4458
TADA
IRA
ISA
UMAP_2
UMAP_1
IRA
ISA
TADA
B
ACSL3
FABP4
VLDLR
CD36
SCARB2
DGAT2
PTGER3
TIMP4
FASN
LIPE
LPL
ANGPTL2
NPR3
ACSL1
IRS1
CEBPB
IGF1
MGLL
IGFBP5
PPARG
APOE
RPS15A
RPL26
RPL12
RPL39
ZNF638
FGFR1
LRP1
LRP5
INSR
GSK3B
ACACB
AACS
ACSS2
DGAT1
Expression
Identity
C
Hypertrophy
N=2393
Hyperplasia
N=2065
UMAP_2
UMAP_1
IRA
ISA
TADA
D
Cell fractions of adipocyte subpopulations
IRA
ISA
TADA
Hypertrophy
Hyperplasia
E
Cells per µl
IRA
ISA
TADA
Hypertrophy
Hyperplasia
F
N=2020
UMAP_2
UMAP_1
FAC1
FAC2
FAC3
G
FBN1
PRG4
MFAP5
HMCN2
FN1
PI16
GAS7
DPP4
KLF3
PLIN2
APOD
IGFBP7
FGF7
PDGFRA
APOE
ADIRF
ACACB
FABP4
Identity
Expression
H
Hypertrophy
Hyperplasia
N=1110
N=910
UMAP_2
UMAP_1
FAC1
FAC2
FAC3
I
Cell fractions of FAC subpopulations
FAC1
FAC2
FAC3
Hypertrophy
Hyperplasia
J
Cells per µl
FAC1
FAC2
FAC3
Hypertrophy
Hyperplasia

Figure 3. Adipocyte and fibroadipogenic cell subpopulations in the subjects with hypertrophic *vs.* hyperplasic adipocytes

(A) UMAP projection showing adipocyte subpopulations in the combined analysis.

(B) Level of expression of maker genes by the different adipocyte subpopulations.

(C) UMAP projections showing differences in adipocyte subpopulations between the hypertrophic and hyperplasic adipose tissues.

(D) Differences in adipocyte subpopulation fractions between the hypertrophic and hyperplasic adipose tissues.

(E) Differences in the tissue concentration of adipocyte subpopulations between the hypertrophic and hyperplasic adipose tissues.

(F) UMAP projection showing fibroadipogenic cell subpopulations in the combined analysis.

(G) Level of expression of maker genes by the different fibroadipogenic cell subpopulations.

(H) UMAP projections showing differences in fibroadipogenic cell subpopulations between the hypertrophic and hyperplasic adipose tissues.

(I) Differences in fibroadipogenic cell subpopulation fractions between the hypertrophic and hyperplasic adipose tissues.

(J) Differences in the tissue concentration of fibroadipogenic cell subpopulations between the hypertrophic and hyperplasic adipose tissues. FAC, fibroadipogenic cells; IRA, insulin-resistant adipocytes; ISA, insulin-sensitive adipocytes; TADA, transcriptionally active developing adipocytes.

Single nuclei RNA-sequencing identified transcriptionally distinct subpopulations of fibroadipogenic cells in hypertrophic and hyperplasic adipose tissue

Re-clustering of fibroadipogenic cells revealed three FAC subpopulations (Figure 3F). As shown in Figure 3G, the FAC3 subpopulation is characterized by the elevated expression of *DPP4*, *FBN1*, *KLF3*, and *FN1*, and therefore strongly resembles a previously identified population of DPP4+ activated fibroblasts[56] which contributes to tissue fibrosis.[57–59] The FAC2 subpopulation expresses high levels of growth factors and growth factor-binding proteins (e.g., *FGF7* and *IGFBP7*), *PLIN2*, and *PDGFRA*, a fibroadipogenic progenitor marker,[60,61] whereas FAC1 expresses the highest levels of *ACACB* (implicated in lipid synthesis and adipogenesis),[62,63] *ADIRF*,[64] and *FABP4* (a marker of mature adipocytes expressed by preadipocytes and associated with adipogenic potential[65]). These results indicate that FAC2 and FAC1 are early fibroadipogenic precursors and preadipocytes, respectively.

Activated fibroblasts (FAC3) are present in higher quantity and fractions in hypertrophied compared to hyperplasic AT, whereas the fractions of FAC2 and FAC1 cells are higher in the hyperplasic AT (Figures 3H and 3I). Furthermore, when expressed *per* volume of AT, early fibroadipogenic precursors (FAC2) and preadipocytes (FAC1) are twice as prevalent in the hyperplasic vs. the hypertrophic AT (Figure 3J).

Adipocyte hypertrophy/hyperplasia is related to differential adipogenic trajectory and transcriptional dynamics of adipocytes and fibroadipogenic cells

After combining all FAC and adipocyte subpopulations and mapping these onto the same UMAP projection, cell trajectory inference was performed to demonstrate the differentiation pathways of fibroadipogenic cells and adipocytes. As shown in Figure 4A, the inferred trajectory for the combined analysis connected the early fibroadipogenic precursor (FAC2) subpopulation to the TADA adipocyte population after passing through the preadipocyte (FAC1) cluster. From there, cell trajectory divided into two branches, leading either to the ISA or the IRA subpopulations of mature adipocytes. RNA velocity analysis of the combined dataset showed consistent results, indicating that cells from the FAC2 subpopulation transitions either to the activated fibroblast (FAC3) or to the FAC1 population and toward the TADA cluster (Figure 4B). Adipocytes from the TADA subpopulation were then predicted to become either ISAs or IRAs. Furthermore, latent time computed based on velocity analysis indicated that mature IRAs were found at later time points compared to mature ISAs, suggesting that IRA adipogenesis occurred at a slower rate compared to that of ISA.

Trajectory analysis in hypertrophied AT demonstrated a single major branch connecting fibroadipocyte cells with fibroblasts and preadipocytes with IRAs after passing through fibroadipocyte cells and TADAs (Figure 4C). RNA velocity analysis indicated that cells of the fibroadipocyte type transition coordinately to the fibrocyte population, while TADAs were predicted to become IRAs (Figure 4D) at relatively low velocity (Figure S3A). In contrast, trajectory analysis in hyperplasic AT did not reveal any major branch connecting fibroadipocytes with fibroblasts (Figure 4E), which was consistent with the absence of organized velocity vectors between fibroadipocytes and fibroblasts (Figure 4F). Instead, one single major trajectory linked fibroadipocytes with ISAs through preadipocytes and TADAs. Furthermore, RNA velocity vectors connecting TADAs to ISAs in the hyperplasic sample (Figure 4F) showed a more organized and rapid transition than those connecting TADAs to IRAs in the hypertrophic AT (Figure 4D), indicating unimpeded and faster adipocyte maturation with AT hyperplasia.

To further assess differential transcript regulation, FAC and adipocytes from hypertrophied and hyperplastic AT were compared to identify genes driving differential velocity expression (Table S5). Rates of transcription, splicing, and degradation of these differential genes were computed (Table S6). Notably, *ADIPOQ-AS1* was found to have nearly six-times higher rate of transcription in the hypertrophic compared to the hyperplasic AT. Spliced-to unspliced ratio showed that the velocity phase portraits (Figure S4) of *ADIPOQ-AS1* were higher in the hypertrophic AT. *ADIPOQ-AS1* levels have been shown to be associated with lower adiponectin[66] and *ADIPOQ-AS* long noncoding RNA administration reduced adiponectin and adipogenesis in mice.[67] In addition, transcription rate of *COL6A3*, which has been associated with insulin resistance,[68] was higher in the hypertrophic AT. Rate of degradation of *PLIN1*, which is involved in the formation of unilocular lipid droplets,[69,70] was also reduced in the hypertrophic AT. Furthermore, velocity analysis also identified *ACACB*—associated with obesity and type 2 diabetes[71]—as a driver gene that is upregulated in the hypertrophic AT (Figure S4).

Hypertrophic and hyperplasic at contain transcriptionally distinct subpopulations of immune cells

Re-clustering of immune cells revealed the presence of NK cells, T cells, and three subpopulations of macrophages, which are characterized by the expression of classical immune cell markers (Figures 5A and 5B). Lipid-associated macrophages (LAM) have been previously identified

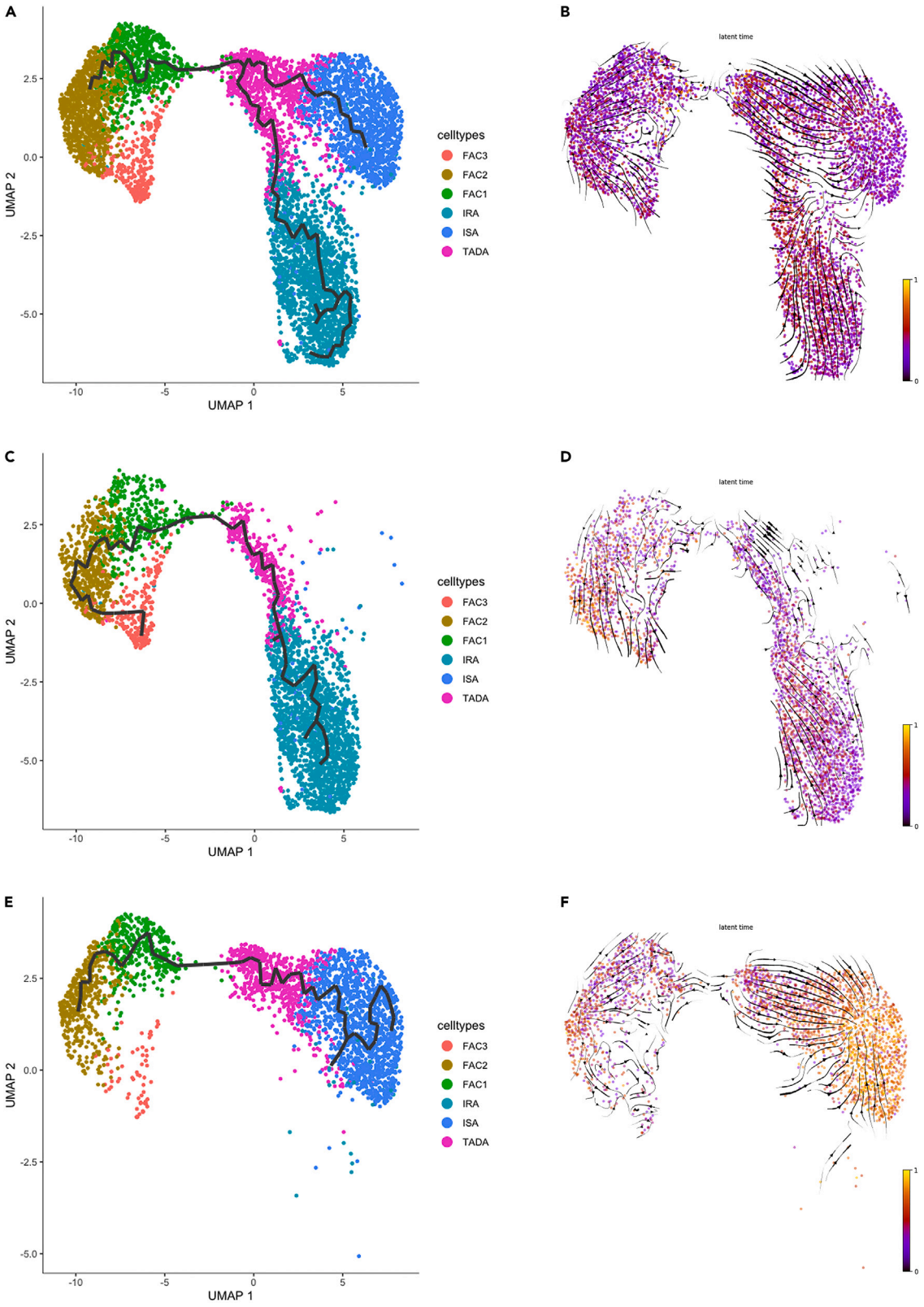
A
B
C
D
E
F
UMAP 1
UMAP 2
celltypes
FAC3
FAC2
FAC1
IRA
ISA
TADA
latent time

Figure 4. Transcriptional dynamics of adipose tissue cells in the patients with hypertrophic vs hyperplasic adipocytes

(A) Cell trajectory of fibroadipogenic cells and adipocytes in the combined analysis.

(B) RNA velocity of fibroadipogenic cells and adipocytes in the combined analysis.

(C) Cell trajectory of fibroadipogenic cells and adipocytes in the hypertrophic adipose tissue.

(D) RNA velocity of fibroadipogenic cells and adipocytes in the hypertrophic adipose tissue.

(E) Cell trajectory of fibroadipogenic cells and adipocytes in the hyperplasic adipose tissue. FAC, fibroadipogenic cells.

(F) RNA velocity of fibroadipogenic cells and adipocytes in the hyperplasic adipose tissue. FAC, fibroadipogenic cells. IRA, insulin-resistant adipocytes; ISA, insulin-sensitive adipocytes; TADA, transcriptionally active developing adipocytes.

(*CD9*+[6,8,72,73] and *TREM2*+[8,9,11,73–75]) and are differentiated by high expression of genes implicated in lipid metabolism (e.g., *LPL*, *FABP5*, and *PLIN2*) (Figures 5C and 5D). Perivascular macrophages (PVM) have also been previously reported and are marked by the expression of *CD163*, *LYVE1*, and *MRC1*.[11,76] Anti-inflammatory macrophages (AIM) express increased levels of genes associated with an anti-inflammatory profile (e.g., *VEGFA*,[77] *STAB1*,[78] and *LILRB5*[79]) and M2 polarization (*DAB2*).[80,81] Compared to the biopsy with hyperplasia, the hypertrophic AT demonstrated a shift in macrophage subpopulations with higher prevalence of AIM and PVM but lower LAM fraction and tissue density (Figures 5E–5G).

Single nuclei RNA-sequencing reveals transcriptional dynamics of macrophage subpopulations in hypertrophic/hyperplasic adipose tissue

Cell trajectory was inferred based on the combined dataset and was shown to connect all three subpopulations of macrophages (Figure S5A). The path of macrophage trajectory was generally parallel to RNA velocity vectors computed using dynamic modeling (Figure S5B), demonstrating consistency between the two methods. LAMs that were transcriptionally more similar to AIMs were predicted to transition rapidly toward the AIM subpopulation. However, in the hypertrophied AT, part of the LAMs which were the furthest apart from the AIM cluster (Figures S5C and S5D) showed reduced RNA velocity (Figures S3B and S3C) and were present at a later point on the latent timescale. This was not the case, however, in hyperplasic AT, in which this region of low RNA velocity (Figure S5D) was not present during LAMs' predicted transition toward the AIM cluster (Figures S5E and S5F).

DISCUSSION

We found that increased adipocyte diameter, as defined by the histological examination of SCAT, was predictor of *in vivo* AT insulin resistance and postprandial NEFA and total fatty acid uptake in the heart. Adipocyte hypertrophy was, however, associated with higher visceral AT DFA partitioning and lower lean tissue DFA partitioning independently of BMI, age and sex. As a result, SCAT fat cell size also predicted lower total postprandial DFA uptake by the liver. To explore potential mechanisms of AT hypertrophy-associated dysmetabolism at a single-cell resolution, we used **snRNA-seq** to perform an unbiased comparison of cellular heterogeneity and transcriptional dynamics of all subcutaneous AT cell types between individuals with AT hypertrophy vs. hyperplasia matched for sex, ethnicity, glucose-tolerance status, BMI, total and percent body fat, as well as waist circumference. We used **snRNA-seq** as a proxy for **scRNA-seq** as the high-lipid containing adipocytes are unsuitable for tradition emulation-base RNA sequencing. Additionally, we used integrated analysis to demonstrate the consistency of AT **snRNA-seq** results between replicates, species, and across different AT regions. Our results highlight significant shifts in cell populations and differentiation trajectories with AT hypertrophy that are consistent with systemic and adipose tissue insulin resistance and postprandial abnormalities of fatty acid metabolism from *in vivo* metabolic testing.

Increased postprandial flux of fatty acids to lean organs from AT metabolic dysfunction has been one of the main diabetogenic mechanisms of obesity promoted over the past two decades.[82–91] The present study demonstrates that adipocyte hypertrophy is independently associated with the postprandial increase in total plasma NEFA uptake in lean organs between 90 and 120 min after meal intake that we previously identified in individuals with overweight and prediabetes.[5] Concurrently, SCAT cell size is also independently associated with the increase in VAT DFA partitioning also previously identified in subjects with prediabetes.[4] This in turn reduces hepatic DFA uptake and curbs total postprandial hepatic fatty acid uptake. Thus, SCAT cell hypertrophy associates with both the deleterious enhanced mobilization of NEFA contributing to liver steatosis[92,93] and a protective increase in DFA storage in intra-abdominal AT. Interestingly, AT NEFA release and VAT DFA partitioning rapidly improve within 2 weeks after bariatric surgery,[94,95] suggesting that these mechanisms are highly dynamic and not uniquely attributable to adipocyte size *per se*. The precise *in vivo* neuro-endocrine effectors of these AT metabolic functions are not fully elucidated, but circulating glucose/insulin, triglyceride-rich lipoprotein levels, glucose-dependent insulinotropic peptide, and AT sympathetic afferent signal are among the identified players.[96] In the present study, we observed a positive relationship between adipocyte size and 6-h postprandial total fatty acid uptake only in the heart, but not in the liver. We also demonstrate that adipocyte size associates with increased visceral AT DFA partitioning and reduced postprandial DFA uptake in the liver, but not in the heart. Thus, adipocyte hypertrophy potentially leads to both pathogenic and adaptive changes in lean organ fatty acid uptake, that variably impact the heart and the liver over the entire postprandial period. The reason for this discrepancy between different organs needs to be investigated in future studies.

In general, AT lipid droplet turnover rate is reduced with obesity, indicating net lipid storage (reviewed in[1]). However, this reduction plateaus in subcutaneous AT at lower fat mass than in visceral AT.[2] Furthermore, there exists an inflection point in the relationship between subcutaneous and visceral AT volume measured by CT beyond which subcutaneous AT growth tends to plateau while visceral AT continues to expand linearly.[3] In light of these results, visceral AT may represent a second line of defense against fat deposition in lean tissues as

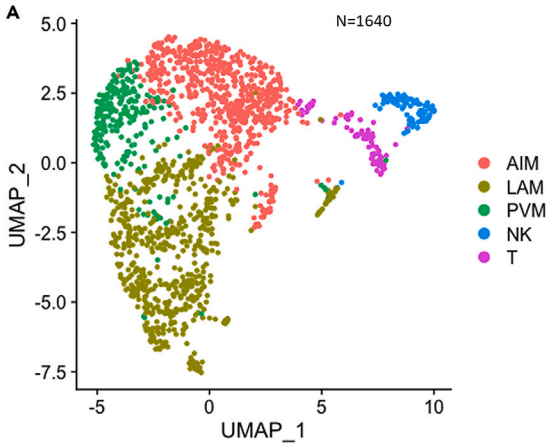
A
N=1640
UMAP_2
UMAP_1
AIM
LAM
PVM
NK
T

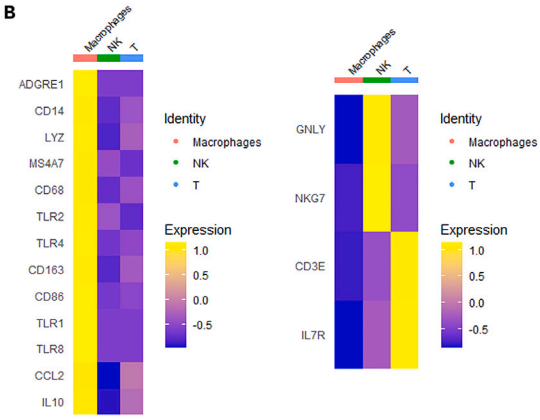
B
Macrophages
NK
T
ADGRE1
CD14
LYZ
MS4A7
CD68
TLR2
TLR4
CD163
CD86
TLR1
TLR8
CCL2
IL10
GNLY
NKG7
CD3E
IL7R
Identity
Expression

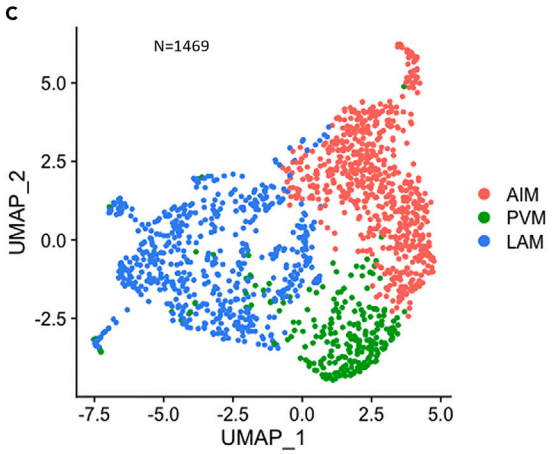
C
N=1469
UMAP_2
UMAP_1
AIM
PVM
LAM

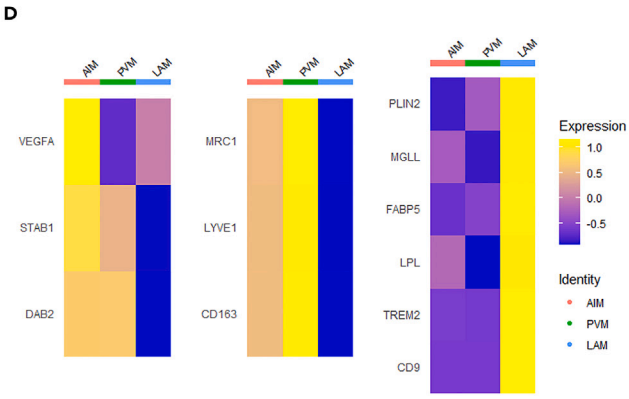
D
AIM
PVM
LAM
VEGFA
STAB1
DAB2
MRC1
LYVE1
CD163
PLIN2
MGLL
FABP5
LPL
TREM2
CD9
Expression
Identity

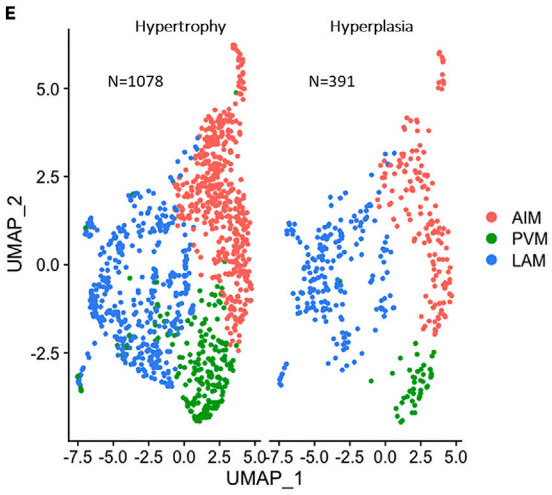
E
Hypertrophy
Hyperplasia
N=1078
N=391
UMAP_2
UMAP_1
AIM
PVM
LAM

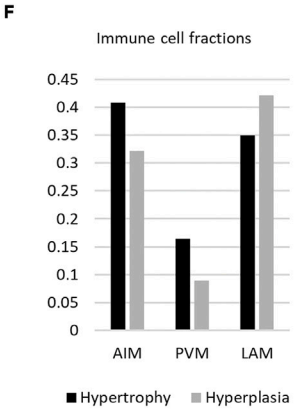
F
Immune cell fractions
AIM
PVM
LAM
Hypertrophy
Hyperplasia

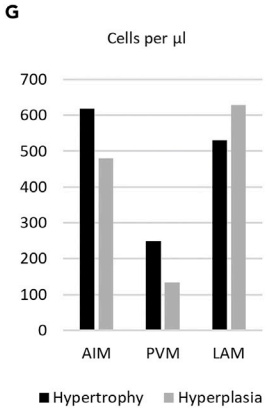
G
Cells per µl
AIM
PVM
LAM
Hypertrophy
Hyperplasia

Figure 5. Single nuclei RNA sequencing of adipose tissue immune cells in patients with hypertrophic vs. hyperplasic adipocytes

(A) UMAP projection showing subtypes of immune cells.

(B) Level of expression of maker genes by the different subtypes of immune cells.

(C) UMAP projection showing macrophage subpopulations in the combined analysis.

(D) Level of expression of maker genes by the different macrophage subpopulations.

(E) UMAP projections showing differences in macrophage subpopulations between the hypertrophic and hyperplasic adipose tissues.

(F) Differences in macrophage subpopulation fractions between the hypertrophic and hyperplasic adipose tissues.

(G) Differences in the tissue concentration of macrophage subpopulations between the hypertrophic and hyperplasic adipose tissues. AIM, anti-inflammatory macrophages; LAM, lipid-associated macrophages; PVM, perivascular macrophages; NK, natural killer cells; T, T lymphocytes.

subcutaneous AT reaches a lipid storage limit. Simpler methods of body composition assessment (such as DXA) usually differentiate visceral from subcutaneous AT only through regression models generated against the gold standards of CT or MRI imaging. However, it is often impractical to manually label thousands of CT slices even using a semi-automatic method. Therefore, we leveraged the ability of deep convolutional neural networks to perform semantic segmentation in order to accurately measure subcutaneous and visceral AT volume and fatty acid uptake on whole-body PET/CT.[19] Our results show that hypertrophied subcutaneous AT is predominantly associated with higher visceral AT DFA storage capacity. Therefore, as the adipogenic potential of subcutaneous AT becomes overwhelmed, subcutaneous adipocytes may undergo hypertrophy with reduced relative capacity to store excess fat, leading to compensatory visceral AT expansion. It may thus be postulated that inter-individual variation in subcutaneous adipogenic potential may lead to differences in whole-body fat distribution and metabolism despite identical total body fat volume. In the present study, we demonstrated that higher fatty acid uptake in lean tissue is a likely mediator of the association between adipocyte hypertrophy and worse HOMA and ADIPO-IR.

The association between adipocyte diameter with postprandial ADIPO-IR was independent of BMI in the multivariate regression model. The ATIRI index, an index of adipose tissue insulin resistance, was associated with adipocyte size, but not with BMI. In a recent meta-analysis (Ye et al., 2021b), we have also shown that adipocyte hypertrophy is associated with dysregulations in glucose and lipid metabolism, ectopic fat accumulation, and cardiovascular endpoints independent of BMI.

As expected, we extracted fewer nuclei *per* gram of tissue from the hypertrophied compared to the hyperplasic SCAT; when we take into account the higher volume of hypertrophied adipocytes, we extracted nuclei from approximately the same fraction of cells in both biopsy samples. Unsupervised clustering identified a number of cell type markers identical to those reported in murine epididymal[11] and human AT.[6,10,13] We also showed good overlap between our data and data from murine AT of different fat depots. Furthermore, the consistent expression of marker genes by different cell types between our replicates and that of external datasets also supports the reliability of our method. Because we matched for BMI and waist circumference, the cellular phenotypes observed between the hypertrophic vs. hyperplasic individuals was not extreme. We nevertheless could observe several cellular features associated with changes in *in vivo* postprandial metabolism.

We found reduced prevalence of FACs – in particular that of FAC1 preadipocytes and FAC2 fibroadipogenic progenitors – *per* volume of AT with fat cell hypertrophy. This is consistent with prior reports of reduced adipogenic potential with adipocyte hypertrophy.[97–100] FAC1 preadipocytes expressed high levels of *ADIRF*, which has been shown to be involved in the initiation of adipogenesis and to act upstream of *PPARG* activation.[64] Furthermore, the fraction of DPP4+ fibroblasts (FAC3)[56–58] is increased with AT hypertrophy, which supports the finding that adipocyte hypertrophy is associated with the thickening of pericellular collagen.[101] In addition, trajectory inference and RNA velocity analyses also revealed that FAC2 fibroadipogenic progenitors in AT hypertrophy are predicted to become FAC fibroblasts instead of FAC1 preadipocytes in AT hyperplasia, thus highlighting the potential role of FAC2 programming in mature adipocyte morphology and AT fibrosis. Because increased pericellular collagen deposition may hinder adipocyte expansion, increased number of fibroblasts may also contribute to ectopic fat accumulation and insulin resistance by limiting further fat storage expansion in hypertrophied subcutaneous adipocytes.

Analyses of RNA velocity shows decreased velocity of adipocyte transformation from the TADA phenotype to mature adipocytes in AT hypertrophy. This finding corroborates the observation that the rate of new adipocyte production is negatively correlated with fat cell size[99] even after controlling for BMI.[100] Furthermore, the fate of adipocyte differentiation also varied between hypertrophy and hyperplasia. In AT hypertrophy, adipocytes from the early TADA stage are destined to become IRA, whereas those in AT hyperplasia are developing into ISA. Furthermore, the fraction and tissue concentration of TADAs are reduced with AT hypertrophy. Integration of the murine epididymal AT dataset by Sárvári et al.[11] also showed the reduction in the number of preadipocytes and TADAs with high fat diet. Moreover, the differences in adipocyte trajectory and transcriptional dynamics measured by the *ex vivo* method are also associated with *in vivo* dysmetabolism. The predominance of IRA vs. ISA is associated with *in vivo* systemic and AT insulin resistance (using ADIPO-IR[16,17,102–104] and ATIRI[15]), postprandial plasma NEFA levels, increased NEFA uptake and metabolism in lean organs, and DFA partitioning away from SCAT and toward visceral AT. Taken together, these results indicate that adipocyte size during periods of lipid storage is predominantly determined by AT adipogenic potential (with higher adipogenic potential favoring expansion consistently through hyperplasia and lower potential quickly leading to hypertrophy); these data also suggest that AT insulin resistance associated with adipocyte hypertrophy may additionally be caused by the presence of a specific phenotype of insulin resistant mature adipocytes as a result of differential developmental commitment at the TADA stage.

Additionally, we showed that hypertrophied AT contained a higher fraction of immune cells, which is in line with the finding by Sárvári et al.[11] showing that hypertrophied AT contains a higher number of infiltrating macrophages[105,106] and results by Emont et al. showing increases in macrophages in mice after high fat diet.[13] Interestingly, despite higher total number of macrophages, hypertrophied AT showed

a shift in macrophage population from the LAM phenotype to higher fractions of AIM and PVM. This result is consistent with the findings that non-inflammatory LAMs[74] play an instrumental role in AT lipid metabolism[8] and in offsetting adipocyte hypertrophy[9] and dyslipidemia.[75] The elevated RNA velocity of the LAM population is also consistent with the high speed of LAM proliferation during AT expansion.[107] In AT hypertrophy, we found a portion of LAMs with low RNA velocity, which may contribute to the observed lower fraction of resident LAMs. Furthermore, we have also observed reduced AT content of endothelial cells and pericytes with hypertrophy, which is consistent with the notion that reduced AT vascularization may, in part, contribute to tissue hypoxia and thus reduced adipocyte differentiation.[108]

In summary, abdominal SCAT hypertrophy is associated with increased postprandial lean tissue fatty acid uptake rates and significant increase in total postprandial fatty acid uptake in the heart. This is a likely mechanism for the association between SCAT hypertrophy and lean tissue insulin resistance. However, SCAT hypertrophy is also associated with increased DFA storage in VAT and reduced partitioning to lean organs. This suggests an important adaptive role of increased VAT DFA storage in moderating the increase in total fatty acid exposure to lean organs, especially the liver, in the context of SCAT hypertrophy. We have also used **snRNA-seq** of frozen human subcutaneous AT with adipocyte hypertrophy and hyperplasia in order to perform an unbiased assessment of the single-cell landscape of all AT cell types, including mature adipocytes. We then uncovered changes in cell clusters and subclusters of adipocytes, FACs, pericytes, endothelial and immune cells as well as differences in transcriptional dynamics and developmental trajectory. These variations detected *ex vivo* are associated with AT insulin resistance, increased VAT DFA trapping, excess exposure of lean tissues to fatty acids, as well as systemic and AT insulin resistance *in vivo*.

Limitations of study

The main limitation of the present study is the lack of assessment of AT transcriptomal dynamics in all participants because of the high cost of the siRNA-seq methodology. This could potentially be achieved in the future with the availability of more affordable methods. Another limitation is the absence of sampling of other AT depots such as visceral or gluteal fat. However, there is good correlation between abdominal subcutaneous vs. other depots adipocyte size.[1] Sex was taken into account in our multivariate analyses of the association of adipocyte hypertrophy and postprandial fatty acid metabolism. However, the influence of sex on AT transcriptomal dynamics in adipocyte hypertrophy could not be performed.

ADDITIONAL RESOURCES

This manuscript reports a pre-specified secondary outcome measurement (abdominal SCAT adipocyte volume) and exploratory analyses of the relationship of this measurement with postprandial fatty acid metabolic outcomes of NCT02808182. Data from this study have partly been reported previously.[4,5]

STAR★METHODS

Detailed methods are provided in the online version of this paper and include the following:

- KEY RESOURCES TABLE
- RESOURCE AVAILABILITY
  - Lead contact
  - Material availability
  - Data and code availability
- EXPERIMENTAL MODEL AND SUBJECTS DETAILS
- METHOD DETAILS
  - Biopsy collection and determination of adipocyte size
  - Selection of matched biopsies
  - Nuclei extraction and purification
  - Single-nuclei capture, library preparation and sequencing
  - Single-nuclei sequence analyses
  - *In vivo* experimental protocols
  - PET/CT analyses
  - Other laboratory assays
- QUANTIFICATION AND STATISTICAL ANALYSIS

SUPPLEMENTAL INFORMATION

Supplemental information can be found online at https://doi.org/10.1016/j.isci.2023.108692.

ACKNOWLEDGMENTS

This work was supported by a grant from the Canadian Institutes of Health Research (CIHR Operating Grant MOP53094). A. C. Carpentier holds the Canada Research Chair in Molecular Imaging of Diabetes. A. Tchernof is co-Director of the Research Chair in Bariatric and Metabolic

Surgery at Laval University. R.Z.Y. receives a studentship award from the Canadian Institutes of Health Research (CIHR Funding Reference Number: 202111FBD-476587-76355). Many thanks to Ms. Anick Turgeon for her help with the final edition of the graphical abstract.

AUTHOR CONTRIBUTIONS

Conceptualization: A.C.C. and R.Z.Y.; methodology: A.C.C., R.Z.Y., H.A.C., and N.G.; software: R.Z.Y.; analysis: R.Z.Y., E.M., C.N., and A.C.C.; investigation: R.Z.Y., E.M., F.F., C.N., H.A.C., and A.C.C.; resources: A.C.C., R.Z.Y., H.A.C., and N.G.; data curation: A.C.C., E.M., F.F., C.N., and R.Z.Y.; writing – original draft: R.Z.Y., A.C.C., and A.T.; visualization: R.Z.Y.; writing – review and editing: R.Z.Y., A.C.C., A.T., E.M., F.F., C.N., H.A.C., and N.G.

DECLARATION OF INTERESTS

A. C. Carpentier received funding by Eli Lilly, HLS Therapeutics, Janssen Inc., Novartis Pharmaceuticals Canada Inc., and Novo Nordisk Canada Inc. as a consultant. A. Tchernof receives research funding from Johnson & Johnson Medical Companies, Medtronic, and GI Windows for studies on bariatric surgery and acted as consultant for Novo Nordisk, Bausch Health and Biotwin. None of these commercial relationships are relevant to the present study.

Received: September 20, 2022
Revised: November 7, 2023
Accepted: December 5, 2023
Published: December 8, 2023

REFERENCES

1. Ye, R.Z., Richard, G., Gévry, N., Tchernof, A., and Carpentier, A.C. (2022). Fat Cell Size: Measurement Methods, Pathophysiological Origins, and Relationships With Metabolic Dysregulations. Endocr. Rev. *43*, 35–60.
2. Spalding, K.L., Bernard, S., Näslund, E., Salehpour, M., Possnert, G., Appelsved, L., Fu, K.Y., Alkass, K., Druid, H., Thorell, A., et al. (2017). Impact of fat mass and distribution on lipid turnover in human adipose tissue. Nat. Commun. *8*, 15253.
3. Sato, S., Demura, S., and Nakai, M. (2015). Storage capacity of subcutaneous fat in Japanese adults. Eur. J. Clin. Nutr. *69*, 933–938.
4. Montastier, É., Ye, R.Z., Noll, C., Bouffard, L., Fortin, M., Frisch, F., Phoenix, S., Guérin, B., Turcotte, É.E., Lewis, G.F., and Carpentier, A.C. (2021). Increased postprandial nonesterified fatty acid efflux from adipose tissue in prediabetes is offset by enhanced dietary fatty acid adipose trapping. Am. J. Physiol. Endocrinol. Metab. *320*, E1093–E1106.
5. Ye, R.Z., Montastier, É., Noll, C., Frisch, F., Fortin, M., Bouffard, L., Phoenix, S., Guérin, B., Turcotte, É.E., and Carpentier, A.C. (2022). Total Postprandial Hepatic Nonesterified and Dietary Fatty Acid Uptake Is Increased and Insufficiently Curbed by Adipose Tissue Fatty Acid Trapping in Prediabetes With Overweight. Diabetes *71*, 1891–1901.
6. Vijay, J., Gauthier, M.F., Biswell, R.L., Louiselle, D.A., Johnston, J.J., Cheung, W.A., Belden, B., Pramatarova, A., Biertho, L., Gibson, M., et al. (2020). Single-cell analysis of human adipose tissue identifies depot and disease specific cell types. Nat. Metab. *2*, 97–109.
7. Rondini, E.A., and Granneman, J.G. (2020). Single cell approaches to address adipose tissue stromal cell heterogeneity. Biochem. J. *477*, 583–600.
8. Magalhaes, M.S., Smith, P., Portman, J.R., Jackson-Jones, L.H., Bain, C.C., Ramachandran, P., Michailidou, Z., Stimson, R.H., Dweck, M.R., Denby, L., et al. (2021). Role of Tim4 in the regulation of ABCA1(+) adipose tissue macrophages and post-prandial cholesterol levels. Nat. Commun. *12*, 4434.
9. Jaitin, D.A., Adlung, L., Thaiss, C.A., Weiner, A., Li, B., Descamps, H., Lundgren, P., Bleriot, C., Liu, Z., Deczkowska, A., et al. (2019). Lipid-Associated Macrophages Control Metabolic Homeostasis in a Trem2-Dependent Manner. Cell *178*, 686–698.e14.
10. Hildreth, A.D., Ma, F., Wong, Y.Y., Sun, R., Pellegrini, M., and O'Sullivan, T.E. (2021). Single-cell sequencing of human white adipose tissue identifies new cell states in health and obesity. Nat. Immunol. *22*, 639–653.
11. Sarvari, A.K., Van Hauwaert, E.L., Markussen, L.K., Gammelmark, E., Marcher, A.B., Ebbesen, M.F., Nielsen, R., Brewer, J.R., Madsen, J.G.S., and Mandrup, S. (2021). Plasticity of Epididymal Adipose Tissue in Response to Diet-Induced Obesity at Single-Nucleus Resolution. Cell Metab *33*, 437–453.e435.
12. Rajbhandari, P., Arneson, D., Hart, S.K., Ahn, I.S., Diamante, G., Santos, L.C., Zaghari, N., Feng, A.C., Thomas, B.J., Vergnes, L., et al. (2019). Single cell analysis reveals immune cell-adipocyte crosstalk regulating the transcription of thermogenic adipocytes. Elife *8*, e49501.
13. Emont, M.P., Jacobs, C., Essene, A.L., Pant, D., Tenen, D., Colleluori, G., Di Vincenzo, A., Jørgensen, A.M., Dashti, H., Stefek, A., et al. (2022). A single-cell atlas of human and mouse white adipose tissue. Nature *603*, 926–933.
14. Wu, H., Kirita, Y., Donnelly, E.L., and Humphreys, B.D. (2019). Advantages of Single-Nucleus over Single-Cell RNA Sequencing of Adult Kidney: Rare Cell Types and Novel Cell States Revealed in Fibrosis. J. Am. Soc. Nephrol. *30*, 23–32.
15. Fabbrini, E., Magkos, F., Conte, C., Mittendorfer, B., Patterson, B.W., Okunade, A.L., and Klein, S. (2012). Validation of a novel index to assess insulin resistance of adipose tissue lipolytic activity in obese subjects. J. Lipid Res. *53*, 321–324.
16. Søndergaard, E., Espinosa De Ycaza, A.E., Morgan-Bathke, M., and Jensen, M.D. (2017). How to Measure Adipose Tissue Insulin Sensitivity. J. Clin. Endocrinol. Metab. *102*, 1193–1199.
17. Gastaldelli, A., Gaggini, M., and DeFronzo, R.A. (2017). Role of Adipose Tissue Insulin Resistance in the Natural History of Type 2 Diabetes: Results From the San Antonio Metabolism Study. Diabetes *66*, 815–822.
18. Labbé, S.M., Grenier-Larouche, T., Croteau, E., Normand-Lauzière, F., Frisch, F., Ouellet, R., Guérin, B., Turcotte, E.E., and Carpentier, A.C. (2011). Organ-specific dietary fatty acid uptake in humans using positron emission tomography coupled to computed tomography. Am. J. Physiol. Endocrinol. Metab. *300*, E445–E453.
19. Ye, R.Z., Noll, C., Richard, G., Lepage, M., Turcotte, É.E., and Carpentier, A.C. (2022). DeepImageTranslator: A free, user-friendly graphical interface for image translation using deep-learning and its applications in 3D CT image analysis. SLAS Technol. *27*, 76–84.
20. Becht, E., McInnes, L., Healy, J., Dutertre, C.A., Kwok, I.W.H., Ng, L.G., Ginhoux, F., and Newell, E.W. (2018). Dimensionality reduction for visualizing single-cell data using UMAP. Nat. Biotechnol. https://doi.org/10.1038/nbt.4314.
21. Muhl, L., Genové, G., Leptidis, S., Liu, J., He, L., Mocci, G., Sun, Y., Gustafsson, S., Buyandelger, B., Chivukula, I.V., et al. (2020). Single-cell analysis uncovers fibroblast heterogeneity and criteria for fibroblast and mural cell identification and discrimination. Nat. Commun. *11*, 3953.
22. Inoue, M., Ishida, T., Yasuda, T., Toh, R., Hara, T., Cangara, H.M., Rikitake, Y., Taira, K., Sun, L., Kundu, R.K., et al. (2010). Endothelial cell-selective adhesion molecule modulates atherosclerosis through plaque angiogenesis and

monocyte-endothelial interaction. Microvasc. Res. *80*, 179–187.
23. Sawano, A., Iwai, S., Sakurai, Y., Ito, M., Shitara, K., Nakahata, T., and Shibuya, M. (2001). Flt-1, vascular endothelial growth factor receptor 1, is a novel cell surface marker for the lineage of monocyte-macrophages in humans. Blood *97*, 785–791.
24. Lip, G.Y., and Blann, A. (1997). von Willebrand factor: a marker of endothelial dysfunction in vascular disorders? Cardiovasc. Res. *34*, 255–265.
25. Nichol, D., and Stuhlmann, H. (2012). EGFL7: a unique angiogenic signaling factor in vascular development and disease. Blood *119*, 1345–1352.
26. Mitchell, T.S., Bradley, J., Robinson, G.S., Shima, D.T., and Ng, Y.S. (2008). RGS5 expression is a quantitative measure of pericyte coverage of blood vessels. Angiogenesis *11*, 141–151.
27. Garin-Shkolnik, T., Rudich, A., Hotamisligil, G.S., and Rubinstein, M. (2014). FABP4 attenuates PPARgamma and adipogenesis and is inversely correlated with PPARgamma in adipose tissues. Diabetes *63*, 900–911.
28. Furuhashi, M., Saitoh, S., Shimamoto, K., and Miura, T. (2014). Fatty Acid-Binding Protein 4 (FABP4): Pathophysiological Insights and Potent Clinical Biomarker of Metabolic and Cardiovascular Diseases. Clin. Med. Insights Cardiol. *8*, 23–33.
29. Hotamisligil, G.S., Johnson, R.S., Distel, R.J., Ellis, R., Papaioannou, V.E., and Spiegelman, B.M. (1996). Uncoupling of obesity from insulin resistance through a targeted mutation in aP2, the adipocyte fatty acid binding protein. Science *274*, 1377–1379.
30. Cai, L., Wang, Z., Ji, A., Meyer, J.M., and van der Westhuyzen, D.R. (2012). Scavenger receptor CD36 expression contributes to adipose tissue inflammation and cell death in diet-induced obesity. PLoS One *7*, e36785.
31. Kennedy, D.J., Kuchibhotla, S., Westfall, K.M., Silverstein, R.L., Morton, R.E., and Febbraio, M. (2011). A CD36-dependent pathway enhances macrophage and adipose tissue inflammation and impairs insulin signalling. Cardiovasc. Res. *89*, 604–613.
32. Sasaki, Y., Ohta, M., Desai, D., Figueiredo, J.L., Whelan, M.C., Sugano, T., Yamabi, M., Yano, W., Faits, T., Yabusaki, K., et al. (2015). Angiopoietin Like Protein 2 (ANGPTL2) Promotes Adipose Tissue Macrophage and T lymphocyte Accumulation and Leads to Insulin Resistance. PLoS One *10*, e0131176.
33. Tabata, M., Kadomatsu, T., Fukuhara, S., Miyata, K., Ito, Y., Endo, M., Urano, T., Zhu, H.J., Tsukano, H., Tazume, H., et al. (2009). Angiopoietin-like protein 2 promotes chronic adipose tissue inflammation and obesity-related systemic insulin resistance. Cell Metab. *10*, 178–188.
34. Kim, J., Lee, S.K., Jang, Y.J., Park, H.S., Kim, J.H., Hong, J.P., Lee, Y.J., and Heo, Y.S. (2018). Enhanced ANGPTL2 expression in adipose tissues and its association with insulin resistance in obese women. Sci. Rep. *8*, 13976.
35. Sugii, S., Olson, P., Sears, D.D., Saberi, M., Atkins, A.R., Barish, G.D., Hong, S.H., Castro, G.L., Yin, Y.Q., Nelson, M.C., et al. (2009). PPARgamma activation in adipocytes is sufficient for systemic insulin sensitization. Proc. Natl. Acad. Sci. USA *106*, 22504–22509.
36. Paschoal, V.A., Walenta, E., Talukdar, S., Pessentheiner, A.R., Osborn, O., Hah, N., Chi, T.J., Tye, G.L., Armando, A.M., Evans, R.M., et al. (2020). Positive Reinforcing Mechanisms between GPR120 and PPARgamma Modulate Insulin Sensitivity. Cell Metab *31*, 1173–1188.e1175.
37. Wang, Y., Nishina, P.M., and Naggert, J.K. (2009). Degradation of IRS1 leads to impaired glucose uptake in adipose tissue of the type 2 diabetes mouse model TALLYHO/Jng. J. Endocrinol. *203*, 65–74.
38. Rondinone, C.M., Wang, L.M., Lonnroth, P., Wesslau, C., Pierce, J.H., and Smith, U. (1997). Insulin receptor substrate (IRS) 1 is reduced and IRS-2 is the main docking protein for phosphatidylinositol 3-kinase in adipocytes from subjects with non-insulin-dependent diabetes mellitus. Proc. Natl. Acad. Sci. USA *94*, 4171–4175.
39. Kovacs, P., Hanson, R.L., Lee, Y.H., Yang, X., Kobes, S., Permana, P.A., Bogardus, C., and Baier, L.J. (2003). The role of insulin receptor substrate-1 gene (IRS1) in type 2 diabetes in Pima Indians. Diabetes *52*, 3005–3009.
40. Danielsson, A., Ost, A., Nystrom, F.H., and Strålfors, P. (2005). Attenuation of insulin-stimulated insulin receptor substrate-1 serine 307 phosphorylation in insulin resistance of type 2 diabetes. J. Biol. Chem. *280*, 34389–34392.
41. Haywood, N.J., Slater, T.A., Matthews, C.J., and Wheatcroft, S.B. (2019). The insulin like growth factor and binding protein family: Novel therapeutic targets in obesity & diabetes. Mol. Metab. *19*, 86–96.
42. Rojas-Rodriguez, R., Lifshitz, L.M., Bellve, K.D., Min, S.Y., Pires, J., Leung, K., Boeras, C., Sert, A., Draper, J.T., Corvera, S., and Moore Simas, T.A. (2015). Human adipose tissue expansion in pregnancy is impaired in gestational diabetes mellitus. Diabetologia *58*, 2106–2114.
43. Kallio, P., Tolppanen, A.M., Kolehmainen, M., Poutanen, K., Lindström, J., Tuomilehto, J., Kuulasmaa, T., Kuusisto, J., Pulkkinen, L., and Uusitupa, M. (2009). Association of sequence variations in the gene encoding insulin-like growth factor binding protein 5 with adiponectin. Int. J. Obes. *33*, 80–88.
44. Farmer, S.R. (2005). Regulation of PPARgamma activity during adipogenesis. Int. J. Obes. *29*, S13–S16.
45. Meruvu, S., Hugendubler, L., and Mueller, E. (2011). Regulation of adipocyte differentiation by the zinc finger protein ZNF638. J. Biol. Chem. *286*, 26516–26523.
46. Du, C., Ma, X., Meruvu, S., Hugendubler, L., and Mueller, E. (2014). The adipogenic transcriptional cofactor ZNF638 interacts with splicing regulators and influences alternative splicing. J. Lipid Res. *55*, 1886–1896.
47. Wang, S., Cao, S., Arhatte, M., Li, D., Shi, Y., Kurz, S., Hu, J., Wang, L., Shao, J., Atzberger, A., et al. (2020). Adipocyte Piezo1 mediates obesogenic adipogenesis through the FGF1/FGFR1 signaling pathway in mice. Nat. Commun. *11*, 2303.
48. Widberg, C.H., Newell, F.S., Bachmann, A.W., Ramnoruth, S.N., Spelta, M.C., Whitehead, J.P., Hutley, L.J., and Prins, J.B. (2009). Fibroblast growth factor receptor 1 is a key regulator of early adipogenic events in human preadipocytes. Am. J. Physiol. Endocrinol. Metab. *296*, E121–E131.
49. Masson, O., Chavey, C., Dray, C., Meulle, A., Daviaud, D., Quilliot, D., Muller, C., Valet, P., and Liaudet-Coopman, E. (2009). LRP1 receptor controls adipogenesis and is up-regulated in human and mouse obese adipose tissue. PLoS One *4*, e7422.
50. Huang, Z., Zhang, M., Plec, A.A., Estill, S.J., Cai, L., Repa, J.J., McKnight, S.L., and Tu, B.P. (2018). ACSS2 promotes systemic fat storage and utilization through selective regulation of genes involved in lipid metabolism. Proc. Natl. Acad. Sci. USA *115*, E9499–E9506.
51. Wang, L., Wang, Y., Meng, Y., Zhang, C., and Di, L. (2018). GSK3-activated STAT5 regulates expression of SFRPs to modulate adipogenesis. FASEB J *32*, 4714–4726.
52. Reggio, A., Rosina, M., Palma, A., Cerquone Perpetuini, A., Petrilli, L.L., Gargioli, C., Fuoco, C., Micarelli, E., Giuliani, G., Cerretani, M., et al. (2020). Adipogenesis of skeletal muscle fibro/adipogenic progenitors is affected by the WNT5a/GSK3/beta-catenin axis. Cell Death Differ. *27*, 2921–2941.
53. Cignarelli, A., Genchi, V.A., Perrini, S., Natalicchio, A., Laviola, L., and Giorgino, F. (2019). Insulin and Insulin Receptors in Adipose Tissue Development. Int. J. Mol. Sci. *20*, 759.
54. Boucher, J., Softic, S., El Ouaamari, A., Krumpoch, M.T., Kleinridders, A., Kulkarni, R.N., O'Neill, B.T., and Kahn, C.R. (2016). Differential Roles of Insulin and IGF-1 Receptors in Adipose Tissue Development and Function. Diabetes *65*, 2201–2213.
55. Loh, N.Y., Neville, M.J., Marinou, K., Hardcastle, S.A., Fielding, B.A., Duncan, E.L., McCarthy, M.I., Tobias, J.H., Gregson, C.L., Karpe, F., and Christodoulides, C. (2015). LRP5 regulates human body fat distribution by modulating adipose progenitor biology in a dose- and depot-specific fashion. Cell Metab. *21*, 262–273.
56. Tabib, T., Morse, C., Wang, T., Chen, W., and Lafyatis, R. (2018). SFRP2/DPP4 and FMO1/LSP1 Define Major Fibroblast Populations in Human Skin. J. Invest. Dermatol. *138*, 802–810.
57. Soare, A., Györfi, H.A., Matei, A.E., Dees, C., Rauber, S., Wohlfahrt, T., Chen, C.W., Ludolph, I., Horch, R.E., Bäuerle, T., et al. (2020). Dipeptidylpeptidase 4 as a Marker of Activated Fibroblasts and a Potential Target for the Treatment of Fibrosis in Systemic Sclerosis. Arthritis Rheumatol. *72*, 137–149.
58. Lee, S.Y., Wu, S.T., Liang, Y.J., Su, M.J., Huang, C.W., Jao, Y.H., and Ku, H.C. (2020). Soluble Dipeptidyl Peptidase-4 Induces Fibroblast Activation Through Proteinase-Activated Receptor-2. Front. Pharmacol. *11*, 552818.
59. Hepler, C., Shan, B., Zhang, Q., Henry, G.H., Shao, M., Vishvanath, L., Ghaben, A.L., Mobley, A.B., Strand, D., Hon, G.C., and Gupta, R.K. (2018). Identification of functionally distinct fibro-inflammatory and adipogenic stromal subpopulations in visceral adipose tissue of adult mice. Elife *7*, e39636.
60. Dani, C., and Pfeifer, A. (2017). The complexity of PDGFR signaling: regulation of adipose progenitor maintenance and adipocyte-myofibroblast transition. Stem Cell Investig. *4*, 28.
61. Burl, R.B., Ramseyer, V.D., Rondini, E.A., Pique-Regi, R., Lee, Y.H., and Granneman, J.G. (2018). Deconstructing Adipogenesis Induced by beta3-Adrenergic Receptor

Activation with Single-Cell Expression Profiling. Cell Metab *28*, 300–309.e4.
62. Yi, X., Wu, P., Liu, J., Gong, Y., Xu, X., and Li, W. (2019). Identification of the potential key genes for adipogenesis from human mesenchymal stem cells by RNA-Seq. J. Cell. Physiol. *234*, 20217–20227.
63. Wang, H., Zhong, J., Zhang, C., Chai, Z., Cao, H., Wang, J., Zhu, J., Wang, J., and Ji, Q. (2020). The whole-transcriptome landscape of muscle and adipose tissues reveals the ceRNA regulation network related to intramuscular fat deposition in yak. BMC Genom. *21*, 347.
64. Ni, Y., Ji, C., Wang, B., Qiu, J., Wang, J., and Guo, X. (2013). A Novel pro-adipogenesis factor abundant in adipose tissues and over-expressed in obesity acts upstream of PPARgamma and C/EBPalpha. J. Bioenerg. Biomembr. *45*, 219–228.
65. Shan, T., Liu, W., and Kuang, S. (2013). Fatty acid binding protein 4 expression marks a population of adipocyte progenitors in white and brown adipose tissues. FASEB J. *27*, 277–287.
66. Spracklen, C.N., Iyengar, A.K., Vadlamudi, S., Raulerson, C.K., Jackson, A.U., Brotman, S.M., Wu, Y., Cannon, M.E., Davis, J.P., Crain, A.T., et al. (2020). Adiponectin GWAS loci harboring extensive allelic heterogeneity exhibit distinct molecular consequences. PLoS Genet. *16*, e1009019.
67. Cai, R., Sun, Y., Qimuge, N., Wang, G., Wang, Y., Chu, G., Yu, T., Yang, G., and Pang, W. (2018). Adiponectin AS lncRNA inhibits adipogenesis by transferring from nucleus to cytoplasm and attenuating Adiponectin mRNA translation. Biochim. Biophys. Acta. Mol. Cell Biol. Lipids *1863*, 420–432.
68. Dankel, S.N., Svärd, J., Matthä, S., Claussnitzer, M., Klöting, N., Glunk, V., Fandalyuk, Z., Grytten, E., Solsvik, M.H., Nielsen, H.J., et al. (2014). COL6A3 expression in adipocytes associates with insulin resistance and depends on PPARgamma and adipocyte size. Obesity *22*, 1807–1813.
69. Grahn, T.H.M., Zhang, Y., Lee, M.J., Sommer, A.G., Mostoslavsky, G., Fried, S.K., Greenberg, A.S., and Puri, V. (2013). FSP27 and PLIN1 interaction promotes the formation of large lipid droplets in human adipocytes. Biochem. Biophys. Res. Commun. *432*, 296–301.
70. Sun, Z., Gong, J., Wu, H., Xu, W., Wu, L., Xu, D., Gao, J., Wu, J.W., Yang, H., Yang, M., and Li, P. (2013). Perilipin1 promotes unilocular lipid droplet formation through the activation of Fsp27 in adipocytes. Nat. Commun. *4*, 1594.
71. Dong, Z., Lei, X., Kujawa, S.A., Bolu, N., Zhao, H., and Wang, C. (2021). Identification of core gene in obese type 2 diabetes patients using bioinformatics analysis. Adipocyte *10*, 310–321.
72. Hill, D.A., Lim, H.W., Kim, Y.H., Ho, W.Y., Foong, Y.H., Nelson, V.L., Nguyen, H.C.B., Chegireddy, K., Kim, J., Habertheuer, A., et al. (2018). Distinct macrophage populations direct inflammatory versus physiological changes in adipose tissue. Proc. Natl. Acad. Sci. USA *115*, E5096–E5105.
73. van Eijk, M., and Aerts, J.M.F.G. (2021). The Unique Phenotype of Lipid-Laden Macrophages. Int. J. Mol. Sci. *22*, 4039.
74. Xu, X., Grijalva, A., Skowronski, A., van Eijk, M., Serlie, M.J., and Ferrante, A.W., Jr. (2013). Obesity activates a program of lysosomal-dependent lipid metabolism in adipose tissue macrophages independently of classic activation. Cell Metab. *18*, 816–830.
75. Aouadi, M., Vangala, P., Yawe, J.C., Tencerova, M., Nicoloro, S.M., Cohen, J.L., Shen, Y., and Czech, M.P. (2014). Lipid storage by adipose tissue macrophages regulates systemic glucose tolerance. Am. J. Physiol. Endocrinol. Metab. *307*, E374–E383.
76. Chakarov, S., Lim, H.Y., Tan, L., Lim, S.Y., See, P., Lum, J., Zhang, X.M., Foo, S., Nakamizo, S., Duan, K., et al. (2019). Two distinct interstitial macrophage populations coexist across tissues in specific subtissular niches. Science *363*, eaau0964.
77. Wheeler, K.C., Jena, M.K., Pradhan, B.S., Nayak, N., Das, S., Hsu, C.D., Wheeler, D.S., Chen, K., and Nayak, N.R. (2018). VEGF may contribute to macrophage recruitment and M2 polarization in the decidua. PLoS One *13*, e0191040.
78. Rantakari, P., Patten, D.A., Valtonen, J., Karikoski, M., Gerke, H., Dawes, H., Laurila, J., Ohlmeier, S., Elima, K., Hübscher, S.G., et al. (2016). Stabilin-1 expression defines a subset of macrophages that mediate tissue homeostasis and prevent fibrosis in chronic liver injury. Proc. Natl. Acad. Sci. USA *113*, 9298–9303.
79. Samaniego, R., Dominguez-Soto, A., Ratnam, M., Matsuyama, T., Sanchez-Mateos, P., Corbi, A.L., and Puig-Kroger, A. (2020). Folate Receptor beta (FRbeta) Expression in Tissue-Resident and Tumor-Associated Macrophages Associates with and Depends on the Expression of PU. Cells *1*, 9.
80. Adamson, S.E., Griffiths, R., Moravec, R., Senthivinayagam, S., Montgomery, G., Chen, W., Han, J., Sharma, P.R., Mullins, G.R., Gorski, S.A., et al. (2016). Disabled homolog 2 controls macrophage phenotypic polarization and adipose tissue inflammation. J. Clin. Invest. *126*, 1311–1322.
81. Figliuolo da Paz, V., Ghishan, F.K., and Kiela, P.R. (2020). Emerging Roles of Disabled Homolog 2 (DAB2) in Immune Regulation. Front. Immunol. *11*, 580302.
82. Lewis, G.F., Carpentier, A., Adeli, K., and Giacca, A. (2002). Disordered fat storage and mobilization in the pathogenesis of insulin resistance and type 2 diabetes. Endocr. Rev. *23*, 201–229.
83. Slawik, M., and Vidal-Puig, A.J. (2007). Adipose tissue expandability and the metabolic syndrome. Genes Nutr. *2*, 41–45.
84. Vidal-Puig, A. (2013). Adipose tissue expandability, lipotoxicity and the metabolic syndrome. Endocrinol. Nutr. *60*, 39–43.
85. Sethi, J.K., and Vidal-Puig, A.J. (2007). Thematic review series: adipocyte biology. Adipose tissue function and plasticity orchestrate nutritional adaptation. J. Lipid Res. *48*, 1253–1262.
86. Ravussin, E., and Smith, S.R. (2002). Increased fat intake, impaired fat oxidation, and failure of fat cell proliferation result in ectopic fat storage, insulin resistance, and type 2 diabetes mellitus. Ann. N. Y. Acad. Sci. *967*, 363–378.
87. Roust, L.R., and Jensen, M.D. (1993). Postprandial free fatty acid kinetics are abnormal in upper body obesity. Diabetes *42*, 1567–1573.
88. Nelson, R.H., Mundi, M.S., Vlazny, D.T., Smailovic, A., Muthusamy, K., Almandoz, J.P., Singh, E., Jensen, M.D., and Miles, J.M. (2013). Kinetics of saturated, monounsaturated, and polyunsaturated fatty acids in humans. Diabetes *62*, 783–788.
89. Basu, A., Basu, R., Shah, P., Vella, A., Rizza, R.A., and Jensen, M.D. (2001). Systemic and regional free fatty acid metabolism in type 2 diabetes. Am. J. Physiol. Endocrinol. Metab. *280*, E1000–E1006.
90. Nelson, R.H., Basu, R., Johnson, C.M., Rizza, R.A., and Miles, J.M. (2007). Splanchnic spillover of extracellular lipase-generated fatty acids in overweight and obese humans. Diabetes *56*, 2878–2884.
91. Almandoz, J.P., Singh, E., Howell, L.A., Grothe, K., Vlazny, D.T., Smailovic, A., Irving, B.A., Nelson, R.H., and Miles, J.M. (2013). Spillover of Fatty acids during dietary fat storage in type 2 diabetes: relationship to body fat depots and effects of weight loss. Diabetes *62*, 1897–1903.
92. Khan, R.S., Bril, F., Cusi, K., and Newsome, P.N. (2019). Modulation of Insulin Resistance in Nonalcoholic Fatty Liver Disease. Hepatology *70*, 711–724.
93. Bril, F., Barb, D., Portillo-Sanchez, P., Biernacki, D., Lomonaco, R., Suman, A., Weber, M.H., Budd, J.T., Lupi, M.E., and Cusi, K. (2017). Metabolic and histological implications of intrahepatic triglyceride content in nonalcoholic fatty liver disease. Hepatology *65*, 1132–1144.
94. Grenier-Larouche, T., Carreau, A.M., Geloën, A., Frisch, F., Biertho, L., Marceau, S., Lebel, S., Hould, F.S., Richard, D., Tchernof, A., and Carpentier, A.C. (2017). Fatty Acid Metabolic Remodeling During Type 2 Diabetes Remission After Bariatric Surgery. Diabetes *66*, 2743–2755.
95. Carreau, A.M., Noll, C., Blondin, D.P., Frisch, F., Nadeau, M., Pelletier, M., Phoenix, S., Cunnane, S.C., Guérin, B., Turcotte, E.E., et al. (2020). Bariatric Surgery Rapidly Decreases Cardiac Dietary Fatty Acid Partitioning and Hepatic Insulin Resistance Through Increased Intra-abdominal Adipose Tissue Storage and Reduced Spillover in Type 2 Diabetes. Diabetes *69*, 567–577.
96. Carpentier, A.C. (2021). 100(th) anniversary of the discovery of insulin perspective: insulin and adipose tissue fatty acid metabolism. Am. J. Physiol. Endocrinol. Metab. *320*, E653–E670.
97. Isakson, P., Hammarstedt, A., Gustafson, B., and Smith, U. (2009). Impaired preadipocyte differentiation in human abdominal obesity: role of Wnt, tumor necrosis factor-alpha, and inflammation. Diabetes *58*, 1550–1557.
98. Park, H.T., Lee, E.S., Cheon, Y.P., Lee, D.R., Yang, K.S., Kim, Y.T., Hur, J.Y., Kim, S.H., Lee, K.W., and Kim, T. (2012). The relationship between fat depot-specific preadipocyte differentiation and metabolic syndrome in obese women. Clin. Endocrinol. *76*, 59–66.
99. Arner, E., Westermark, P.O., Spalding, K.L., Britton, T., Rydén, M., Frisén, J., Bernard, S., and Arner, P. (2010). Adipocyte turnover: relevance to human adipose tissue morphology. Diabetes *59*, 105–109.
100. Lessard, J., Laforest, S., Pelletier, M., Leboeuf, M., Blackburn, L., and Tchernof, A. (2014). Low abdominal subcutaneous preadipocyte adipogenesis is associated with visceral obesity, visceral adipocyte

hypertrophy, and a dysmetabolic state. Adipocyte *3*, 197–205.

101. Vargas, G., Chandalia, M., Jiang, Y., Davila, H., Motamedi, M., and Abate, N. (2013). Heterogeneity in subcutaneous adipose tissue morphology and metabolic complications in overweight and obese women. Metab. Syndr. Relat. Disord. *11*, 276–282.
102. Gastaldelli, A., Harrison, S.A., Belfort-Aguilar, R., Hardies, L.J., Balas, B., Schenker, S., and Cusi, K. (2009). Importance of changes in adipose tissue insulin resistance to histological response during thiazolidinedione treatment of patients with nonalcoholic steatohepatitis. Hepatology *50*, 1087–1093.
103. Gastaldelli, A., Cusi, K., Pettiti, M., Hardies, J., Miyazaki, Y., Berria, R., Buzzigoli, E., Sironi, A.M., Cersosimo, E., Ferrannini, E., and Defronzo, R.A. (2007). Relationship between hepatic/visceral fat and hepatic insulin resistance in nondiabetic and type 2 diabetic subjects. Gastroenterology *133*, 496–506.
104. Lomonaco, R., Ortiz-Lopez, C., Orsak, B., Webb, A., Hardies, J., Darland, C., Finch, J., Gastaldelli, A., Harrison, S., Tio, F., and Cusi, K. (2012). Effect of adipose tissue insulin resistance on metabolic parameters and liver histology in obese patients with nonalcoholic fatty liver disease. Hepatology *55*, 1389–1397.
105. Zhang, H.M., Chen, L.L., Wang, L., Xu, S., Wang, X., Yi, L.L., Chen, D., Wu, Z.H., Zhang, J.Y., Liao, Y.F., and Shang, J. (2009). Macrophage infiltrates with high levels of Toll-like receptor 4 expression in white adipose tissues of male Chinese. Nutr. Metab. Cardiovasc. Dis. *19*, 736–743.
106. Cancello, R., Henegar, C., Viguerie, N., Taleb, S., Poitou, C., Rouault, C., Coupaye, M., Pelloux, V., Hugol, D., Bouillot, J.L., et al. (2005). Reduction of macrophage infiltration and chemoattractant gene expression changes in white adipose tissue of morbidly obese subjects after surgery-induced weight loss. Diabetes *54*, 2277–2286.
107. Muir, L.A., Kiridena, S., Griffin, C., DelProposto, J.B., Geletka, L., Martinez-Santibañez, G., Zamarron, B.F., Lucas, H., Singer, K., O' Rourke, R.W., and Lumeng, C.N. (2018). Frontline Science: Rapid adipose tissue expansion triggers unique proliferation and lipid accumulation profiles in adipose tissue macrophages. J. Leukoc. Biol. *103*, 615–628.
108. Engin, A. (2017). Adipose Tissue Hypoxia in Obesity and Its Impact on Preadipohcytes and Macrophages: Hypoxia Hypothesis. Adv. Exp. Med. Biol. *960*, 305–326.
109. Galarraga, M., Campión, J., Muñoz-Barrutia, A., Boqué, N., Moreno, H., Martínez, J.A., Milagro, F., and Ortiz-de-Solórzano, C. (2012). Adiposoft: automated software for the analysis of white adipose tissue cellularity in histological sections. J. Lipid Res. *53*, 2791–2796.
110. Goldrick, R.B. (1967). Morphological changes in the adipocyte during fat deposition and mobilization. Am. J. Physiol. *212*, 777–782.
111. Lun, A.T.L., Riesenfeld, S., Andrews, T., Dao, T.P., Gomes, T.; participants in the 1st Human Cell Atlas, and Marioni, J.C. (2019). EmptyDrops: distinguishing cells from empty droplets in droplet-based single-cell RNA sequencing data. Genome Biol. *20*, 63.
112. Lun, A.T.L., McCarthy, D.J., and Marioni, J.C. (2016). A step-by-step workflow for low-level analysis of single-cell RNA-seq data with Bioconductor. F1000Res. *5*, 2122.
113. 10x Genomics, Chromium Next GEM Single Cell 5' Reagent Kits V2 (Dual Index) User Guide (2020.
114. Hao, Y., Hao, S., Andersen-Nissen, E., Mauck, W.M., 3rd, Zheng, S., Butler, A., Lee, M.J., Wilk, A.J., Darby, C., Zager, M., et al. (2021). Integrated analysis of multimodal single-cell data. Cell *184*, 3573–3587.e29.
115. Qiu, X., Mao, Q., Tang, Y., Wang, L., Chawla, R., Pliner, H.A., and Trapnell, C. (2017). Reversed graph embedding resolves complex single-cell trajectories. Nat. Methods *14*, 979–982.
116. La Manno, G., Soldatov, R., Zeisel, A., Braun, E., Hochgerner, H., Petukhov, V., Lidschreiber, K., Kastriti, M.E., Lönnerberg, P., Furlan, A., et al. (2018). RNA velocity of single cells. Nature *560*, 494–498.
117. Bergen, V., Lange, M., Peidli, S., Wolf, F.A., and Theis, F.J. (2020). Generalizing RNA velocity to transient cell states through dynamical modeling. Nat. Biotechnol. *38*, 1408–1414.
118. Kunach, M., Noll, C., Phoenix, S., Guérin, B., Baillargeon, J.P., Turcotte, E.E., and Carpentier, A.C. (2015). Effect of Sex and Impaired Glucose Tolerance on Organ-Specific Dietary Fatty Acid Metabolism in Humans. Diabetes *64*, 2432–2441.
119. Coggan, A.R., Kisrieva-Ware, Z., Dence, C.S., Eisenbeis, P., Gropler, R.J., and Herrero, P. (2009). Measurement of myocardial fatty acid esterification using [1-11C]palmitate and PET: comparison with direct measurements of myocardial triglyceride synthesis. J. Nucl. Cardiol. *16*, 562–570.
120. Iozzo, P., Bucci, M., Roivainen, A., Någren, K., Järvisalo, M.J., Kiss, J., Guiducci, L., Fielding, B., Naum, A.G., Borra, R., et al. (2010). Fatty acid metabolism in the liver, measured by positron emission tomography, is increased in obese individuals. Gastroenterology *139*, 846–856. 856.e1-6.
121. Brassard, P., Frisch, F., Lavoie, F., Cyr, D., Bourbonnais, A., Cunnane, S.C., Patterson, B.W., Drouin, R., Baillargeon, J.P., and Carpentier, A.C. (2008). Impaired plasma nonesterified fatty acid tolerance is an early defect in the natural history of type 2 diabetes. J. Clin. Endocrinol. Metab. *93*, 837–844.
122. Normand-Lauzière, F., Frisch, F., Labbé, S.M., Bherer, P., Gagnon, R., Cunnane, S.C., and Carpentier, A.C. (2010). Increased postprandial nonesterified fatty acid appearance and oxidation in type 2 diabetes is not fully established in offspring of diabetic subjects. PLoS One *5*, e10956.
123. Carpentier, A.C., Frisch, F., Cyr, D., Généreux, P., Patterson, B.W., Giguère, R., and Baillargeon, J.P. (2005). On the suppression of plasma nonesterified fatty acids by insulin during enhanced intravascular lipolysis in humans. Am. J. Physiol. Endocrinol. Metab. *289*, E849–E856.
124. Ci, X., Frisch, F., Lavoie, F., Germain, P., Lecomte, R., van Lier, J.E., Bénard, F., and Carpentier, A.C. (2006). The effect of insulin on the intracellular distribution of 14(R,S)-[18F]Fluoro-6-thia-heptadecanoic acid in rats. Mol. Imaging Biol. *8*, 237–244.
125. Loening, A.M., and Gambhir, S.S. (2003). AMIDE: a free software tool for multimodality medical image analysis. Mol. Imaging *2*, 131–137.
126. Ménard, S.L., Croteau, E., Sarrhini, O., Gélinas, R., Brassard, P., Ouellet, R., Bentourkia, M., van Lier, J.E., Des Rosiers, C., Lecomte, R., and Carpentier, A.C. (2010). Abnormal in vivo myocardial energy substrate uptake in diet-induced type 2 diabetic cardiomyopathy in rats. Am. J. Physiol. Endocrinol. Metab. *298*, E1049–E1057.
127. Plourde, C.É., Grenier-Larouche, T., Caron-Dorval, D., Biron, S., Marceau, S., Lebel, S., Biertho, L., Tchernof, A., Richard, D., and Carpentier, A.C. (2014). Biliopancreatic diversion with duodenal switch improves insulin sensitivity and secretion through caloric restriction. Obesity *22*, 1838–1846.
128. Steele, R. (1959). Influences of glucose loading and of injected insulin on hepatic glucose output. Ann. N. Y. Acad. Sci. *82*, 420–430.

STAR★METHODS

KEY RESOURCES TABLE

REAGENT or RESOURCE	SOURCE	IDENTIFIER
Chemicals, Peptides, and Recombinant Proteins		
NaCl 0.9% Irrigation, 1000mL	Baxter	JF7634
Formaldehyde, 10%	Sigma-Aldrich	HT 501128
Ethanol, 100%	Commercial Alcohols Inc.	P016EAAN
Paraffin	Paraplast Surgipath	39601006
Hematoxylin	Fisherbrand	245–651
Eosin	Fisherbrand	245–827
HEPES	Sigma-Aldrich	H3375
$MgCl_2$	Fisher Scientific	M33
KCl	Fisher Scientific	P217
Sucrose	Fisher Scientific	S5
NP-40	ThermoFisher	FNN0021
RNase inhibitor	Sigma-Aldrich	3335399001
BSA	Sigma-Aldrich	9048-46-8
DAPI	Fisher	62248
PBS	Sigma-Aldrich	806552
Aprotinin	Sigma-Aldrich	A6279
[7,7,8,8-^{2}H]-palmitate	Cambridge Isotopes Laboratories Inc.	DLM-6033-MPT
NaH[^{13}C]O_3	Cambridge Isotopes Laboratories Inc.	CLM-441-MPT-PK
[1,1,2,3,3-^{2}H]glycerol	Cambridge Isotopes Laboratories Inc.	DLM-1229-MPT-PK
[U-^{13}C]-palmitate	Cambridge Isotopes Laboratories Inc.	CLM-3934
25% human albumin	Alburex 25	02274663
LC-MS grade water	Fisher Scientific	51140
MTBSTFA (with 1% t-BDMCS)	Millipore-Sigma	77377-52-7
Imidazole	Millipore-Sigma	288-32-4
Critical Commercial assays		
Chromium Next GEM Single Cell 5′ Kit v2, 16 rxns	10X Genomics	PN-1000263
Chromium Next GEM Chip K Single Cell Kit, 48 rxns	10X Genomics	PN-1000286
Library Construction Kit, 16 rxns	10X Genomics	PN-1000190
5′ Feature Barcode Kit, 16 rxns	10X Genomics	PN-1000256
Glucose measurement kit	Wako	439–90901
NEFA measurement kit	Wako	995–34791 999–34691 993–35191 991–34891
TG measurement kit	Wako	990–02991 994–02891
C-peptide, GIP, Glucagon, GLP-1 total, Insulin, Leptin, PYY, hormone panel	Millipore	HMH3-34K-07

(*Continued on next page*)

Continued

REAGENT or RESOURCE	SOURCE	IDENTIFIER
Software and Algorithms		
Adiposoft	https://ImageJ.net/plugins/adiposoft	v1.14
Raw single nuclei RNA sequencing dataset generated	Ye et al.	NCBI GEO database, accession number: GSE230912
Cell Ranger		v6.0.2
EmptyDrops		
scDblFinder		
Scran	Bioconductor	
R		v4.1.0
Seurat		v4.0
Monocle3		
velocyto		v0.17
scVelo		v0.2.3
Python		v3.7
AMIDE		v1.0.5
DeepImageTranslator	Ye et al.	v2.0
NDP.view2	U12388-01	U12388-01
Genome Reference Consortium Human Build 38		PRJNA31257
Others		
Needle, 14G	Covidien	8881200011
Syringe, 20mL	Beckton Dickinson	309661
Nylon mesh, 55µm	Fisher Scientific	08-801-15
Microcentrifuge tube, 1.5mL	Ultident	48-C150-CS
Microcentrifuge tube, 0.5mL	Ultident	17-T330-6N
NanoZoomer 2.0-RS	Hamamatsu	
Horizon DXA System	Hologic	
BD FACS Aria III	BD	
Hydra ECF/ICF	Xitron Technologies	
ECLIPSE Ti-E Inverted microscope	Nikon	
Luminex xMAP-based immunoassays	Millipore	
Accusoft Advantage, glucose monitor	Roche, USA	
Refrigerated Centrifuge	Fisher Scientific	AccuSpin 3R
Gas Chromatograph	Agilent Technologies, Avondale, PA	7890A
Waters Quattro Micro, mass spectrometer	Waters	
Gemini TF PET/CT scanner	Philips	
[^{11}C]-palmitate, radiotracer	CIMS	
[^{18}F]-FTHA, radiotracer	CIMS	
DB-5ms Ultra Inert Intuvo GC column	Agilent Technologies, Avondale, PA	

RESOURCE AVAILABILITY

Lead contact

Further information and requests for resources and reagents should be directed to and will be fulfilled by the lead contact, Dr. André C. Carpentier, Division of Endocrinology, Faculty of Medicine, *University of Sherbrooke*, 3001, 12th Ave North, Sherbrooke, Quebec, Canada J1H 5N4 – Tel: 1-819-564-5243; Fax: 1-819-564-5292; e-mail: Andre.Carpentier@USherbrooke.ca.

Material availability

No new material was generated from this study.

Data and code availability

(1) Data: The raw sequencing data have been deposited in the NCBI Gene Expression Omnibus (GEO) database with following accession number: GSE230912.
(2) Code: The complete lists of all markers for cell types and subpopulations can be found in Supplementary Excel files (S1_Cell_type_-markers.cvs; S2_Adipocyte_Markers.cvs; S3_FACs_markers.cvs; S4_Macrophages_markers.cvs).

EXPERIMENTAL MODEL AND SUBJECTS DETAILS

Informed written consent was obtained, in accordance with the Declaration of Helsinki, and the protocol received approval from the Human Ethics of Research Committee of the *Center de Recherche du Center hospitalier universitaire de Sherbrooke*. Subjects characteristics are described in Table S1. The cohort used for AT biopsy selection included 21 subjects (11 men and 10 women) with impaired glucose tolerance (IGT)—defined as glycemia levels of 7.8–11.1 mmol/L on two separate 2h-post 75g OGTTs—and 19 healthy individuals (9 men and 10 women) with normal glucose tolerance (NGT)—defined as fasting glycemia <5.6 mM, 2h-post 75g OGTTs <7.8 mmol/L, and HbA1c < 5.8%. Participants were aged between 47 and 74. All women were post-menopausal. Those with active disease, except well-controlled hypertension or mild dyslipidemia, or a contraindication for temporary cessation of anti-hypertensive drugs or statins were excluded from the study. Subjects demonstrating clinically significant cardiovascular, renal, or hepatic or uncontrolled thyroid disorder, having medical history of other major illnesses, or taking medications affecting lipid or carbohydrate metabolism that could not be rapidly discontinued (e.g., fibrates, thiazolidinediones, or beta-blockers) or who participated in any research trial involving radiation exposure within the past 12 months were excluded. Smokers and individuals drinking more than 2 alcoholic beverages/day were also excluded.

Two Caucasian males with normal glucose tolerance (fasting glycemia <5.6 mM, 2h-post 75g OGTTs <7.8 mM, and HbA1c < 5.8%) matched for BMI, waist circumference and total fat mass, but with different abdominal subcutaneous fat cell size (FCS) were selected. As shown in Figure S1, participants had a large difference in adipocyte diameter (2.2 standard deviation [SD] difference), but similar BMI (0.21 SD), waist circumference (0.14 SD), total fat mass (0.14 SD), and percent fat mass (0.52 SD). Although it would have been interesting to expand the snRNA-seq data to the whole dataset, such analyses were beyond the scope of the present study.

METHOD DETAILS

Biopsy collection and determination of adipocyte size

Biopsy samples of abdominal subcutaneous AT (2 per subject) were obtained through needle aspiration under local anesthesia with 2% Xylocaine. Samples (100–300 mg) were rinsed with a sterile 0.9% saline solution for a maximum of 3 min to remove fibrin and blood, and immediately frozen in liquid nitrogen and stored at −80°C. A small portion (50 mg) of biopsy samples was not flash frozen and was used for histological analysis. After fixation in 10% formaldehyde for 24–48 h and storage in 70% ethanol at 4°C, the sample was embedded in paraffin. Histological sections were made with a thickness of 5 μm and stained with hematoxylin and eosin. Slides were digitized with a NanoZoomer scanner (NanoZoomer 2.0-RS; Hamamatsu, Japan) at a magnification of 40X. Images were then analyzed with Adiposoft 1.14[109] to measure adipocyte cross-sectional area. Thresholds for minimum and maximum cell diameters were set to 30 μm and 150 μm to minimize erroneous identification of regions not belonging to adipocytes. An average of ∼400 cells were analyzed *per* participant. Mean adipocyte volume was calculated from average fat cell diameter and the standard deviation of fat cell diameter using the formula by Goldrick et al.[110] Due to the large size of their lipid droplet, adipocytes occupy nearly the entirety of the tissue volume in SCAT (Figure S2A). Therefore, for each sample, we used the mean adipocyte volume as a surrogate to determine the total volume occupied by all cells from which the nuclei were extracted and sequenced. This total tissue volume allowed us to compute the number of cells *per* volume of AT. Figure S2B shows that compared to the sample with adipocyte hypertrophy, hyperplasic AT has approximately twice the number of adipocytes, FACs, endothelial cells, and pericytes *per* volume of tissue.

Selection of matched biopsies

Biopsy samples were selected for nuclei extraction and **snRNA-seq** from two participants matched for sex, BMI, fat mass (determined with DEXA scan) and waist circumference, but having the largest difference in adipocyte size.

Nuclei extraction and purification

Frozen biopsy samples were transferred into 1.5 mL microcentrifuge tubes on ice to which 50 μL of nuclei extraction buffer (NEB) (10 mM HEPES, 1.5 mM $MgCl_2$, 10 mM KCl, 250 mM sucrose, 0.1% NP-40, and 0.2 U/μL RNase inhibitor [Sigma, 3335399001]) were added. Sterile 0.5 mL microcentrifuge tubes were fitted into the 1.5 mL microcentrifuge tubes, allowing samples to be homogenized with 12 strokes with rotation, while maintaining the samples on ice. After addition of 3 mL of NEB, samples were incubated on ice for 1 min with gentle mixing followed by centrifugation at 1000 x g for 10 min at 4°C. With the supernatant removed, the nuclei pellet was resuspended in 500 μL of nuclei resuspension buffer (NRB) (0.5% BSA, 0.2 U/μL RNase inhibitor [Sigma, 3335399001], and 20 μg/mL DAPI [Fisher, 62248] in PBS). The nuclei

suspension was then filtered through a 55 μm nylon mesh and observed under a fluorescence microscope for nuclei integrity and absence of clumps. The filtered suspension was then purified using FACS sorting (BD FACS Aria III, BD, Franklin Lakes) for DAPI+ nuclei. All plasticware had been coated with 4% BSA in PBS overnight at 4°C.

Single-nuclei capture, library preparation and sequencing

Single nuclei were captured using Chromium Next GEM Single Cell 5′ v2 according to the manufacturer's instructions (10X Genomics, Pleasanton). Around 10 000 nuclei were loaded into the reaction chip. Sequencing was done with NextSeq 500/550 High Output Kit v2 aiming at a target depth of 20 000 reads/nucleus, with read lengths of 26 cycles (read 1), 10 cycles (i7 index), 10 cycles (i5 index), and 120 cycles (read 2).

Single-nuclei sequence analyses

Single-nuclei sequences were first aligned to the complete human genome (GRCh38) with Cell Ranger 6.0.2. For quality control, empty droplets were first inferred from count matrices and filtered out using EmptyDrops[111] at an FDR threshold of 0.01. Doublet scores were then computed for each nucleus with scDblFinder in Scran.[112] Considering an expected multiplet rate of 0.8% *per* 1000 nuclei,[113] droplets containing doublets were removed such that only 94% of nuclei with the lowest doublet scores were retained. Finally, only genes expressed in at least 3 cells were retained and all nuclei with less than 200 UMIs were removed. Dimensionality reduction, clustering, and visualization of the filtered count matrices were done using Seurat version 4.0 [114] in R 4.1.0. The 2 000 most variable genes were extracted and used for dimensionality reduction with principal component analysis (PCA). The resulting principal components (PCs) were used to compute UMAP embeddings and perform Louvain clustering with Seurat.[114] Trajectory inference was performed using Monocle3.[115] For RNA velocity computation, velocyto 0.17[116] was used to identify spliced, unspliced, and ambiguous transcripts from the aligned sequence based on the human genome (GRCh38). The resulting annotated count matrix was filtered with the same aforementioned quality control procedures and employed for RNA velocity analyses and latent time inference with generalized dynamical modeling using scVelo 0.2.3[117] in Python 3.7. For comparative and integrated analyses with publicly available single-nuclei datasets, we used our count matrices as the reference dataset for transfer anchor discovery and mapped previously published sequence data onto our reference clusters and UMAP embeddings using Seurat.[114]

To directly compare sequencing data across species and AT compartments and thus assess the replicability of AT single-nuclei RNA seq, we first gathered two publicly available single nuclei datasets described by Rajbhandari et al.[12] and Sárvári et al.[11] The dataset by Rajbhandari et al. was generated using collagenase-digested fresh inguinal AT from 8 to 10-week-old mice, whereas the dataset by Sárvári et al. was produced from frozen epididymal AT from 10-week-old mice fed with low-fat diet (LFD) vs. high-fat diet (HFD) for 18 weeks. We used our own single-nuclei dataset as the reference dataset to generate transfer anchors for the two murine datasets, which allowed us to transfer the murine nuclei into our cell population clusters and to map them onto our UMAP projection. For both transferred datasets, we were able to identify all the major cell types and cell subpopulations (Figures S6A–S6C). All identified cell clusters were located in the same regions on the UMAP projection not only within the two transferred murine datasets, but also with their counterparts from the human reference dataset. Figure S6D illustrates that, compared to LFD mice, mice fed with HFD showed significant reduction in the number of AIM, TADA, and FAC1 preadipocytes and an increase in the number of LAM in their epididymal AT, consistent with the results reported by the authors.[11] Finally, we compared the expression of cell type-specific markers between the three datasets and showed strong concordance between the level of expression of these markers in different cell types across all datasets (Figures S6E–S6G).

In vivo experimental protocols

Participants underwent two standardized postprandial protocols (A and B) performed in random order after 3 days of an isocaloric diet with maintenance of their regular physical activities and avoidance of strenuous exercise. These protocols and results were reported in previous publications.[4,5] Upon arrival after a 12-h overnight fast, anthropometric measurements (including height, weight, and waist circumference) were taken. Fat mass and lean mass were quantified using dual-energy X-ray absorptiometry (DEXA; Hologic DXA scanner, Hologic Inc., Bedford, MA) and via electrical bioimpedance (Hydra ECF/ICF; Xitron Technologies, San Diego, CA). An intravenous (I.V.) catheter was inserted in the forearm for infusions, while another catheter was placed in the contralateral arm, maintained in a heating pad (~55°C) for blood sampling. Blood samples were collected in Na_2EDTA-coated tubes containing aprotinin (10 μL/mL; A6279, Sigma-Aldrich, Ontario, Canada), which inhibits *in vitro* proteolysis. At time 0 of each protocol, a standardized 906 kcal liquid meal (400 mL, composed of 33 g of fat, 34 g of protein and 101 g of carbohydrates; *i.e.*, 33%, 17%, 50% of calories, respectively) was consumed over 20 min.[118]

Tracer methods

In protocol A, we used [^{11}C]-palmitate positron emission tomography (PET) dynamic acquisition 90 min after the standard meal intake[5] to determine myocardial[119] and hepatic uptake, oxidation and esterification of plasma NEFA, as well as hepatic NEFA release in VLDL-TG.[120] Ninety minutes after ingestion of the liquid meal, [^{11}C]-palmitate (~185 MBq) was administered intravenously over 30 s with dynamic list mode PET scanning for 30 min (18 × 10, 6 × 30, and 6 × 240 s) preceded by computed tomography (CT) acquisition (40 mA) centered on the thoracoabdominal segment. Arterial input function were assessed from individual image acquisitions (Table S7).

In protocol B, we measured dietary fatty acid (DFA) partitioning and spillover using a combination of oral and I.V. stable isotopic tracers and oral [^{18}F]-FTHA positron emission tomography (PET). A constant I.V. infusion of [7,7,8,8-^{2}H]-palmitate (Cambridge Isotopes Laboratories Inc., 0.01 μmol/kg/min in 100 mL of 25% human albumin) was administered from time −60 min (in the fasting state) to time +360 min (after

meal intake).[121–123] We employed the oral [^{18}F]-FTHA method to determine whole-body DFA partitioning with PET.[18] Ingested [^{18}F]-FTHA is absorbed in the intestines and reaches the circulation as chylomicron-TG through the thoracic duct, and the subsequent hydrolysis of [^{18}F]-FTHA-containing chylomicron-TG is assumed to be identical to that of naturally occurring chylomicron-TG. Approximatively 70 MBq [^{18}F]-FTHA[124] was mixed with olive oil, encapsulated in gel capsules (T.U.B. Enterprises), and administered orally at time 0 min with the liquid meal. At time 360 min, whole-body PET/CT acquisition was performed in the supine position to measure [^{18}F]-FTHA whole-body partitioning.[18] The maximal gastrointestinal tract radioactivity exposure for oral [^{18}F]-FTHA administration was estimated at 2.35 mSv at the stomach. Total radioactivity exposure by study participants after all protocols was inferior to 9.77 mSv. All tracers were tested for sterility and pyrogenicity.

PET/CT analyses

For dynamic thoracic scans in protocol A, ROIs were drawn in the left ventricular cavity, myocardium, and liver using AMIDE (version 1.0.5; A Medical Image Data Examiner; http://amide.sourceforge.net).[125] Hepatic and cardiac NEFA uptake, oxidation, and esterification rates, as well as hepatic rate of NEFA release in TG were determined using multicompartmental models previously published for the heart[119] and liver.[120]

For whole-body scans in protocol B, 10 transverse CT slices were randomly selected for manual image labeling of subcutaneous AT (in red), visceral AT (in green), and other tissues (in blue). Transfer learning was carried out by training a deep convolutional neural network with a U-net architecture that had been previously trained to perform semantic CT segmentation using our DeepImageTranslator software[19] for a total of 100 epochs. This specialized neural network was applied for fully automatic semantic segmentation of 8084 CT slices from all study participants. The generated semantic segmentation maps were applied to calculate the volume of AT and to compute AT uptake of [^{18}F]-FTHA using co-registered PET scans. Tissue partitioning of DFA was computed as previous described.[4] We are aware that 18F radioactivity does spill over into adjacent visceral adipose tissues for PET acquisitions. Therefore, in this study, we used deep learning to measure visceral adipose tissue volume from the CT acquisitions (not affected by 18F radioactivity spillover), but we manually selected perirenal (visceral) adipose tissue regions. As described in our previous studies, these regions are remote enough from GI 18F radioactivity spillover to get VAT-specific PET acquisitions for radioactivity measurement to extrapolate to the entire visceral depot.

To accurately determine AT volume, we first randomly selected 10 transverse CT slices from whole-body PET/CT scans for manual image labeling. We then carried out transfer learning by training a deep convolutional neural network that had been previously trained to perform semantic CT segmentation using our DeepImageTranslator software.[19] This allowed accurate, fully automatic semantic segmentation of 8084 CT slices and measurement of AT volume in the subcutaneous and visceral compartments in the entire study cohort of 40 participants.

Other laboratory assays

Glucose, total NEFA, and TG were measured as described.[126] Plasma adiponectin, insulin, and leptin were measured using Luminex xMAP-based immunoassays (Millipore, Etobicoke, ON, Canada). The Matsuda index was calculated as previously described.[127] Homeostasis model assessment of IR (HOMA-IR) was also calculated as an alternative index of insulin resistance as fasting plasma insulin (U/L) × fasting plasma glucose (mmol/L)/22.5. Fasting and postprandial AT insulin resistance (ADIPO-IR) were computed as plasma insulin (pmol/L) × plasma NEFA (mmol/L) at the fasting state and at 120 min, respectively.[16,17] Plasma appearance rates of palmitate ($Ra_{palmitate}$) and total NEFA (Ra_{NEFA}) were calculated with the Steele's non-steady-state equations[128] as previously described.[4,95] Adipose Tissue Insulin Resistance Index (ATIRI) was calculated as the reduction in the Ra_{NEFA} divided by change in plasma insulin from 0 to 120 min.[15]

QUANTIFICATION AND STATISTICAL ANALYSIS

The variables analyzed in this study were pre-specified and registered in ClinicalTrials.gov (trial number: NCT02808182), this includes variables in Table 1 (insulin sensitivity, partitioning of DFA, and rates of NEFA metabolism in the heart and liver). Adipose tissue cell size was also included as a secondary outcome measurement. The effects of sex, glucose tolerance status, and their interaction were corrected for multiple comparisons in post-hoc analyses. No simple t-test was used in this study. Analyses were performed using IBM SPSS Statistics 26.0 for Windows (IBM, Armonk, NY) or GraphPad Prism 8.0 for Windows (GraphPad Software, San Diego, CA). Details of the statistical tests are indicated in Figure and table legends.